Astronomy & Astrophysics manuscript no. output
January 21, 2025

Evolution of the near-core rotation frequency of 2,497 intermediate-mass stars from their dominant gravito-inertial mode[⋆]

Conny Aerts[1,2,3], Timothy Van Reeth[1], Joey S. G. Mombarg[4,1,5], and Daniel Hey[6]

[1] Institute of Astronomy, KU Leuven, Celestijnenlaan 200D, B-3001 Leuven, Belgium
e-mail: `conny.aerts@kuleuven.be`
[2] Department of Astrophysics, IMAPP, Radboud University Nijmegen, PO Box 9010, 6500 GL Nijmegen, The Netherlands
[3] Max Planck Institute for Astronomy, Königstuhl 17, 69117 Heidelberg, Germany
[4] IRAP, Université de Toulouse, CNRS, UPS, CNES, 14 avenue Édouard Belin, F-31400 Toulouse, France
[5] Université Paris-Saclay, Université de Paris, Sorbonne Paris Cité, CEA, CNRS, AIM, 91191 Gif-sur-Yvette, France
[6] Institute for Astronomy, University of Hawai'i, Honolulu, HI 96822, USA

Received XXX / Accepted XXX

ABSTRACT

Context. The sparsely sampled time-series photometry from *Gaia* Data Release 3 (DR3) led to the discovery of more than 100,000 main-sequence non-radial pulsators. The majority of these were further scrutinised by uninterrupted high-cadence space photometry assembled by the Transiting Exoplanet Survey Satellite (TESS).

Aims. We combine *Gaia* DR3 and TESS photometric light curves to estimate the internal physical properties of 2,497 gravity-mode pulsators. We perform asteroseismic analyses with two major aims: 1) to measure the near-core rotation frequency and its evolution during the main sequence and 2) to estimate the mass, radius, evolutionary stage, and convective core mass from stellar modelling.

Methods. We rely on asteroseismic properties of *Kepler* γ Doradus and Slowly Pulsating B stars to derive the cyclic near-core rotation frequency, $f_{\rm rot}$, of the *Gaia*-discovered pulsators from their dominant prograde dipole gravito-inertial pulsation mode. Further, we investigate the impact of adding $f_{\rm rot}$ as extra asteroseismic observable aside from the luminosity and effective temperature on the outcome of grid-based modelling from rotating stellar models.

Results. We offer a recipe based on linear regression to deduce $f_{\rm rot}$ from the dominant gravito-inertial mode frequency, which we show to be applicable to prograde dipole modes in the sub-inertial regime, having an amplitude above 4 mmag. By applying it to 2497 pulsators with such a mode, we increase the sample of intermediate-mass dwarfs with such an asteroseismic observable by a factor of 4. We use the estimate of $f_{\rm rot}$ to deduce spin parameters between 2 and 6, while the sample's near-core rotation rates range from 0.7% to 25% of the critical Keplerian rate. We use $f_{\rm rot}$, along with the *Gaia* effective temperature and luminosity to deduce the (convective core) mass, radius, and evolutionary stage from grid modelling based on rotating stellar models. We derive a decline of $f_{\rm rot}$ with a factor of two during the main-sequence evolution for this population of field stars, which covers a mass range from 1.3 $M_\odot$ to 7 $M_\odot$. We find observational evidence for an increase in the radial order of excited gravity modes as the stars evolve. For 307 pulsators, we derive an upper limit of the radial differential rotation between the convective core boundary and the surface from *Gaia*'s `vbroad` measurement and find values up to 5.4.

Conclusions. Our recipe to deduce the near-core rotation frequency from the dominant prograde dipole gravito-inertial mode detected in the independent *Gaia* and TESS light curves is easy to use and facilitates applications to large samples of pulsators, mapping their angular momentum and evolutionary stage in the Milky Way.

Key words. Asteroseismology – Waves – Stars: oscillations (including pulsations) – Stars: interiors – Stars: rotation – Stars: evolution

1. Introduction

The internal rotation of stars continues to be one of the major uncertain ingredients in the theory of stellar evolution (Maeder 2009). The dominant transport processes happening in the interiors of stars rely on poorly calibrated expressions involving the gradient of the angular rotation profile. To compute this gradient throughout the evolution of the star, the so-called shellular approximation introduced by Zahn (1992) is often adopted. Relying on this formulation, the profile of $\mathrm{d}\Omega(r)/\mathrm{d}r$ is used to evaluate the element and angular momentum processes in the stellar interior (e.g., Chaboyer & Zahn 1992; Heger et al. 2000; Maeder & Meynet 2000).

Over the past decade, asteroseismology (Aerts et al. 2010) has been a game changer in the study of stellar rotation. Progress on the internal rotation of stars relied on the detection and interpretation of non-radial oscillation modes probing the deepest layers of stars. Dupret et al. (2009) provided theoretical predictions on the capacity of dipole mixed modes to probe the central regions of evolved low-mass stars, while Miglio et al. (2008) and Bouabid et al. (2013) described the properties of gravity and gravito-inertial modes in young intermediate-mass dwarfs. These theoretical studies were turned into practical tools thanks to space asteroseismology (Hekker & Christensen-Dalsgaard

---

[⋆] Data files with the *Gaia* identification number, the near-core rotation frequency, the (convective core) mass, the evolutionary stage, the radius, the dominant oscillation frequency in the co-rotating frame, the spin parameter of the dominant mode, a lower limit for the surface rotation frequency, and an upper limit for the near-core to surface rotation for the stars with these latter two quantities, are all available at the CDS via anonymous ftp to cdsarc.cds.unistra.fr (130.79.128.5) or via https://cdsarc.cds.unistra.fr/viz-bin/cat/J/A+A/ ???/A???

2017; García & Ballot 2019; Córsico et al. 2019; Aerts 2021; Kurtz 2022, for recent overviews).

Accurate values of the angular core or near-core rotation frequencies for thousands of stars were deduced. This was achieved from dipole mixed modes in subgiants and red giants (measuring the core value of the rotation, $\Omega_{\rm core}$, see Beck et al. 2011; Bedding et al. 2011; Beck et al. 2012; Deheuvels et al. 2012; Mosser et al. 2012, 2014, 2015; Gehan et al. 2018) and from dipole gravity or gravito-inertial modes in dwarfs (measuring the near-core value, $\Omega_{\rm near-core}$, just outside the convective core, see Degroote et al. 2010; Pápics et al. 2012, 2014; Kurtz et al. 2014; Saio et al. 2015; Van Reeth et al. 2015b, 2016; Ouazzani et al. 2017; Pápics et al. 2017; Saio et al. 2018). The diagnostic observables used to deduce the measurements of the internal rotation are either rotationally-split multiplets or period spacing patterns of mixed modes or gravity modes affected by the Coriolis acceleration (cf., Aerts et al. 2019, for a review of the methodologies). From the stars that also have a measurement of the angular envelope rotation frequency ($\Omega_{\rm env}$) it was further established that strong (near-)core to envelope coupling occurs, keeping the level of differential rotation ($\Omega_{\rm (near-)core}/\Omega_{\rm env}$) modest during the two longest phases of stellar evolution (Deheuvels et al. 2015; Triana et al. 2015; Van Reeth et al. 2018; Li et al. 2020; Ouazzani et al. 2020; Saio et al. 2021; Li et al. 2024). Further, it was established that the core rotation at the time of central helium exhaustion is in agreement with the rotation of white dwarfs (Hermes et al. 2017; Aerts et al. 2019). Moreover, $\Omega_{\rm (near-)core}/\Omega_{\rm env}$ increases strongly during hydrogen shell burning, reaching values up to 20 (Deheuvels et al. 2014; Di Mauro et al. 2016; Triana et al. 2017; Deheuvels et al. 2020; Li et al. 2024).

Thanks to asteroseismology, our understanding of how angular momentum transport and angular momentum loss slow down the (core) rotation after exhaustion of the central hydrogen has improved dramatically (Fuller et al. 2019; Eggenberger et al. 2019a,b; Moyano et al. 2023a). These novel transport theories comply with the asteroseismic measurements of the internal rotation for thousands of evolved stars of low and intermediate mass. For the longest phase of stellar evolution, however, we only have measurements of $\Omega_{\rm near-core}$ and $\Omega_{\rm env}$ or $\Omega_{\rm surf}$, the latter being the angular rotation frequency at the stellar surface, for less than 100 dwarfs (Li et al. 2020; Pedersen et al. 2021; Pedersen 2022a). These observables cover the mass range of $[1.3, 9]\,{\rm M}_\odot$ and span a broad interval of measured near-core rotation rates (up to about $30\,\mu$Hz, Aerts 2021). As a consequence, our understanding of angular momentum transport during core hydrogen burning is still limited, despite progress over the past five years (Fuller et al. 2019; Eggenberger et al. 2022; Bétrisey et al. 2023; Moyano et al. 2023b, 2024).

Here, our aim is to enlarge the sample of dwarfs with an estimate of the near-core rotation frequency and to study how it evolves in time during the main-sequence phase. We wish to deduce $d\Omega/dt$ in the transition zone from the convective core to the radiative envelope as stars evolve from the zero-age-main-sequence (ZAMS) to the terminal-age-main sequence (TAMS). We achieve this by relying on a sample of thousands of new gravity-mode pulsators discovered from Data Release 3 (DR3) of the *Gaia* space mission (Gaia Collaboration et al. 2023; Aerts et al. 2023). Hey & Aerts (2024) confirmed the pulsational nature of these stars on the basis of independently assembled light curves from the Transiting Exoplanet Survey Satellite (TESS). The sample of gravity-mode pulsators with both *Gaia* DR3 and TESS data in the public domain is 23 times larger than the *Kepler* sample of dwarfs with measurements of $\Omega_{\rm near-core}$ (Mombarg et al. 2024b).

We work towards our goal by relying on two well-established properties of main-sequence gravity-mode pulsators deduced from *Kepler* space-based photometry: 1) the majority of such pulsators reveals dominant prograde dipole modes (Van Reeth et al. 2016; Li et al. 2020); 2) the dominant mode in their amplitude spectra reveals a clear shift towards higher frequency according to their near-core rotation rate (Pápics et al. 2017; Aerts & Tkachenko 2024). Here, we bring these two properties together and come up with a regression formula for the near-core rotation frequency from a measurement of the dominant oscillation frequency of the *Kepler* gravity-mode pulsators (Sect. 2). We apply our recipe to the new sample of confirmed gravity-mode pulsators discovered from *Gaia* and validated by TESS (Sect. 3). We perform grid modelling based on the near-core rotation frequency and the *Gaia* effective temperature and luminosity as non-seismic observables and compare the outcome with published evolutionary grid modelling without an asteroseismic estimate of $\Omega_{\rm near-core}$ (Sect. 4). We end with conclusions and the prospect of deriving an asteroseismic measurement of the near-core rotation frequency for millions of dwarfs across the Milky Way from future combined *Gaia* DR4 and TESS data (Sect. 5).

2. A recipe for the near-core rotation frequency from a prograde dipole gravito-inertial mode

Gaia DR3 led to the discovery of more than 100,000 new candidate (non-)radial pulsators. Their dominant frequency have an amplitude above about 4 mmag (Gaia Collaboration et al. 2023). Among the new non-radial pulsators, Aerts et al. (2023) selected those with an amplitude below 35 mmag and dominant frequency in the range $[0.7,3.2]\,{\rm d}^{-1}$. These two extra criteria were found to be effective in selecting the γ Doradus (γ Dor) and Slowly Pulsating B (SPB) star candidates among the overall sample presented by Gaia Collaboration et al. (2023). The global stellar parameters of these 15,062 candidate gravity-mode pulsators were found to be in good agreement with those of confirmed and well-studied *Kepler* pulsators of these two kinds (Aerts et al. 2023).

Hey & Aerts (2024) revisited the sample of more than 100,000 candidate main-sequence pulsators classified by Gaia Collaboration et al. (2023). They extracted light curves for almost 60,000 of them from TESS Full Frame Images (FFIs) in the public domain. These densely sampled TESS light curves allowed them to confirm the dominant frequency found in the sparsely sampled *Gaia* DR3 time-series photometry for the majority of them. Hey & Aerts (2024) then reclassified the pulsators with a TESS FFI light curve. They came up with a cleaner sub-sample of gravity-mode pulsators among the multiperiodic variables, as improvement with respect to the Aerts et al. (2023) study.

Here, we consider a sub-sample of 15,692 pulsators classified by Hey & Aerts (2024) with a probability above 50% to be either a γ Dor or SPB star or a hybrid pressure/gravity-mode pulsator. Mombarg et al. (2024b) determined the mass, radius, and evolutionary stage of these 15,692 pulsators from evolutionary grid modelling. This was done by matching the stars' *Gaia* DR3 effective temperature and luminosity with those predicted from a grid of rotating stellar models calibrated by asteroseismology of *Kepler* gravity-mode pulsators, covering the mass range from $1.3\,{\rm M}_\odot$ to $9\,{\rm M}_\odot$.

For our study, we rely on the dominant pulsation mode of these 15,692 stars found consistently in the *Gaia* and TESS light curves to assess their cyclic near-core rotation frequency, denoted here for simplicity as $f_{\rm rot} \equiv \Omega_{\rm near-core}/2\pi$. In order to achieve this, we first recall some general properties of well-studied *Kepler* gravity-mode pulsators.

2.1. Basic properties of gravito-inertial modes in dwarfs

Main-sequence pulsators of γ Dor or SPB type exhibit low-frequency gravity modes of high radial-order, n, excited by either the flux blocking mechanism or the κ mechanism (Pamyatnykh 1999; Guzik et al. 2000; Bouabid et al. 2013; Xiong et al. 2016; Szewczuk & Daszyńska-Daszkiewicz 2017). The majority of these pulsators experience moderate to fast rotation, which brings the oscillation modes into the sub-inertial regime, where both buoyancy and the Coriolis force act together as restoring forces (Aerts et al. 2019; Aerts & Tkachenko 2024). Such modes are called gravito-inertial modes, while modes in slow rotators restored by buoyancy alone are pure gravity modes.

In the asymptotic frequency limit, where the pulsation frequency in the co-rotating frame, $f_{\rm co}$, is much smaller than the Brunt-Väisälä frequency, N, and in the Traditional Approximation of Rotation (TAR; e.g., Lee & Saio 1987; Townsend 2003), we have

$$f_{\rm co} = \frac{\sqrt{\lambda_{km\nu}}}{\Pi_0\left(n+\alpha_g\right)}, \tag{1}$$

where $\lambda_{km\nu}$ is the eigenvalue of the Laplace tidal equation for a mode labelled as (k, m) having spin parameter $\nu = 2f_{\rm rot}/f_{\rm co}$, α_g is a phase term dependent on the boundaries of the pulsation mode cavity denoted by the positions r_1 and r_2, and the buoyancy radius

$$\Pi_0 = \frac{2\pi^2}{\int_{r_1}^{r_2}\frac{N(r)}{r}{\rm d}r}. \tag{2}$$

For non-rotating stars, gravity modes are labelled by indices (l, m, n), where l and $|m| \leq l$ denote the degree and azimuthal order of the spherical harmonic Y_l^m describing the displacement vector of the mode. In this work, we define prograde and retrograde modes as having $m > 0$ and $m < 0$, respectively, while zonal modes have $m = 0$. In order to encompass a single mode classification procedure for rotating pulsators, Lee & Saio (1997) defined a suitable labelling scheme based on one unique integer index k because l is not suitable to capture all mode families. The value of k is able to represent all families of solutions to the Laplace tidal equation, which describes the oscillations when the vertical component of the Coriolis acceleration is taken into account, but not the horizontal component. In this labelling scheme, zero or positive values of k correspond to modes having a counterpart of the harmonic degree $l = |m| + k$ in the limit of no rotation. On the other hand, negative k values stand for retrograde modes that do not have any counterpart in the non-rotating case (see also Townsend 2003, for more details on mode classification schemes in rotating pulsators). Our study is focused on stars with $k \geq 0$ modes. In particular, zonal dipole gravity modes are labelled as $(k, m) = (1, 0)$, tesseral quadrupole retrograde gravity modes have $(k, m) = (1, -1)$, while prograde sectoral dipole gravity or gravito-inertial modes have $(k, m) = (0, 1)$, all of which occur in Fig. 1 discussed below.

The condition that the mode frequencies must be well below N is fulfilled for γ Dor and SPB stars, as shown by Aerts et al. (2021, see their Fig. 1). Moreover, Aerts et al. (2017), Aerts et al. (2021), and Pedersen (2022a) deduced the spin parameters of the identified modes of γ Dor and SPB pulsators and found $\nu \geq 1$ for almost all modes in the γ Dor stars and for the majority of them in SPB stars, justifying the use of the TAR in general terms for such pulsators (see Mathis 2013, for extensive discussions on the TAR criteria).

In the limit of high radial order $n \gg 1$ (corresponding to the limit of low frequencies), gravity or gravito-inertial modes of the same (k, m) and consecutive radial order n obey a regular pattern. This is predicted theoretically (Miglio et al. 2008; Bouabid et al. 2013; Van Reeth et al. 2015a; Ouazzani et al. 2017) and observed in photometry of single and binary pulsators assembled with the Convection, Rotation, and exoplanetary Transits (CoRoT), *Kepler* or TESS space telescopes (e.g., Degroote et al. 2010; Pápics et al. 2012, 2014; Kurtz et al. 2014; Saio et al. 2015; Van Reeth et al. 2015b; Keen et al. 2015; Pápics et al. 2017; Szewczuk & Daszyńska-Daszkiewicz 2018; Sekaran et al. 2020; Wu et al. 2020; Li et al. 2020; Szewczuk et al. 2021; Pedersen et al. 2021; Garcia et al. 2022; Kemp et al. 2024). These publications revealed the regular mode patterns detected in the space photometry to allow for mode identification. For the γ Dor stars, most of the observed modes identified as $(k, m) = (0, 1)$ in these publications have radial order $n \in [10, 100]$ (Li et al. 2020), while SPB stars typically have $(k, m) = (0, 1)$ modes with $n \in [10, 50]$ excited (Szewczuk & Daszyńska-Daszkiewicz 2017).

As elaborated by Aerts & Tkachenko (2024), the Coriolis force is more important than the the centrifugal force in the calculation of the modes for γ Dor and SPB stars. This is due to the mode energy being dominated by the region adjacent to the convective core, where the rotational deformation due to the centrifugal force is modest (Mathis & Prat 2019; Henneco et al. 2021; Dhouib et al. 2021a,b). Moreover, the horizontal components of the displacement vector of the modes are typically an order of magnitude larger than the vertical ones (De Cat & Aerts 2002). All of these properties together imply that the TAR is well justified, unless the stars rotate close to their critical rate. We discuss and evaluate this latter condition in Sect. 4.

2.2. Identification of the dominant mode of the *Kepler* gravity-mode pulsators

The combined *Kepler* gravity-mode pulsator samples analysed by Li et al. (2020), Pedersen et al. (2021), and Pedersen (2022b) reveal period-spacing patterns of prograde dipole modes for 610 of the 634 stars in the combined sample (96.2%). For 428 of these, that is 67.5% of the sample, the dominant mode was part of the detected pattern. When only stars with dominant pulsation amplitudes larger than 4 mmag are considered among these *Kepler* pulsators, which is the amplitude detection threshold for the discovery of the *Gaia* DR3 gravity-mode pulsators, this fraction increases to 84.7%.

Hence, in the remainder of this work we rely on the fact that the large majority among the dominant frequencies of well-characterised *Kepler* γ Dor and SPB stars correspond to a mode with $(k, m) = (0, 1)$. While doing so, we keep in mind that about 15% of the dominant frequencies may belong to a mode with another identification of (k, m).

2.3. A regression formula for the internal rotation frequency

In the case of modes with $k = 0$ in moderate- to fast-rotating stars, that is, with $\nu \gg 1$, theory predicts that $\lambda_{km\nu} \approx m^2$ (e.g., Townsend 2003). This leads to a quasi-linear relation between the observed cyclic gravity-mode frequencies f_{nkm} and the near-

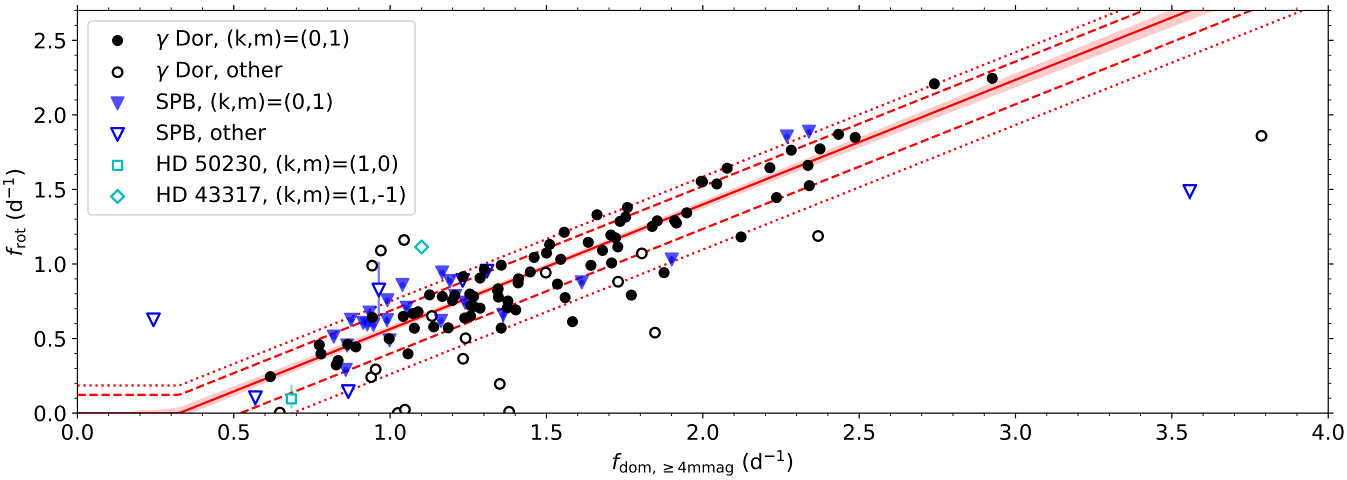

Fig. 1: The near-core rotation frequency $f_{\rm rot}$ plotted as a function of the dominant mode frequency for those *Kepler* gravity-mode pulsators having an observed amplitude above 4 mmag ($f_{\rm dom,\,\geq 4\,mmag}$) from the samples of Li et al. (2020) and Pedersen et al. (2021). Stars are drawn as γ Dor pulsator if they have $T_{\rm eff} < 8500$ K and $\Pi_0 < 0.7$ d and as SPB star otherwise. When invisible, the error bars are smaller than the symbol sizes. The linear relation (red line) given by Eq. (4) was computed for the 105 stars having a dominant $(k, m) = (0, 1)$ mode with observed frequency above 0.35 d^{-1} and with $\nu > 1$ (full symbols). The shaded area shows the 1-σ uncertainty region for this relation. The two pulsators indicated in cyan come from short CoRoT light curves (Degroote et al. 2010; Pápics et al. 2012). As the other open symbols, they were not used in the regression. The dashed (dotted) lines mark the 1-σ confidence interval for $f_{\rm rot}$ derived from the residuals with respect to the red line, excluding (including) stars with modes having $(k, m) \neq (0, 1)$ or $\nu < 1$.

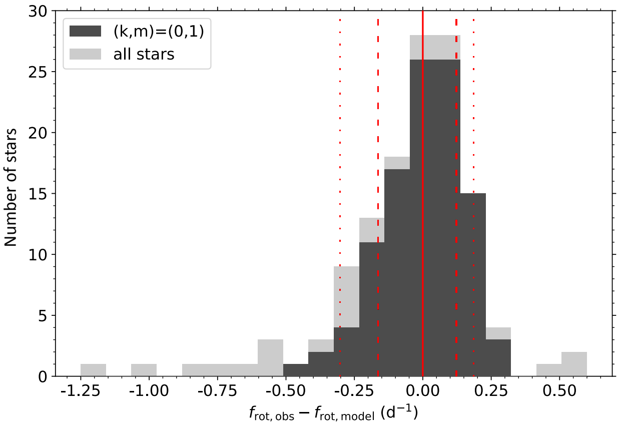

Fig. 2: Residuals from the linear fit described by Eq. (4) for the selected *Kepler* pulsators used in Fig. 1. The distribution of modes with $(k, m) = (0, 1)$, $\nu > 1$, and observed frequency above 0.35 d^{-1} is shown in dark grey, wile the distribution of all dominant modes with amplitude $\geq$ 4 mmag is shown in light grey. The full, dashed, and dotted lines indicate the same relation and confidence intervals as those in Fig. 1.

core rotation frequency $f_{\rm rot}$:

$$f_{\rm nkm} = f_{\rm co} + m f_{\rm rot} \approx \frac{m}{\Pi_0 \left(n + \alpha_g\right)} + m f_{\rm rot}, \tag{3}$$

which has also been found observationally (e.g. Van Reeth et al. 2016; Pápics et al. 2017; Li et al. 2020; Audenaert & Tkachenko 2022). Here, we wish to exploit this relationship in the context of the newly discovered *Gaia* gravity-mode pulsators, whose observed dominant cyclic mode frequencies, $f_{\rm dom}$, are consistent in the DR3 and TESS data and which have amplitudes above 4 mmag. An earlier similar idea was put forward by Sepulveda et al. (2022) and Sepulveda et al. (2023) in the context of the exoplanet host stars 51 Eridani and HR 8799, which are both γ Dor pulsators. These authors considered an averaged frequency value among the dominant modes to infer the near-core rotation frequency in an empirical way by considering the sample of Li et al. (2020), without relying on the theory-based Eq. (3) as we do here.

To quantify the observational relation between $f_{\rm rot}$ and $f_{\rm dom}$ we fit a linear model to the *Kepler* results found for the homogeneously studied samples of γ Dor and SPB pulsators from Li et al. (2020) and Pedersen et al. (2021). In light of the application to the *Gaia* discovered gravity-mode pulsators, we only select the *Kepler* pulsators with dominant pulsation amplitude above 4 mmag and identified as $(k, m) = (0, 1)$, that is only stars with a dominant dipole prograde mode. Moreover, we demand their dominant mode to occur in the sub-inertial regime, where $\nu > 1$. In this way, we find the following regression fit based on the 100 γ Dor stars and 5 SPB stars with dominant prograde dipole mode in the sub-inertial regime of observed amplitude above 4 mmag with asteroseismic modelling from *Kepler*:

$$f_{\rm rot} = 0.836^{+0.023}_{-0.027} f_{\rm dom} - 0.272^{+0.041}_{-0.036}\ {\rm d}^{-1}, \tag{4}$$

where all of $f_{\rm rot}$, $f_{\rm dom}$ and $1/\Pi_0$ are expressed in d^{-1}. This fit is illustrated by the full red line in Fig. 1. The strong correlation between $f_{\rm rot}$ and $f_{\rm dom}$ is reflected by the Pearson correlation coefficient, which has a value of 0.942.

We applied a bootstrap analysis on the residuals of the fit in Eq. (4) and find that the estimated rotation frequency values have uncertainties σ_- and σ_+ of -0.164 d^{-1} and $+0.123$ d^{-1}, respectively. The results for this confidence interval are graphically depicted in Fig. 2 by the dashed lines. If we also take into account the residuals with respect to the regression line for the $\sim 20\%$ sample stars that have pulsations with other geometries $(k, m) \neq (0, 1)$ or in the super-inertial regime ($\nu < 1$), we find uncertainties σ_- and σ_+ of $-0.302\,\mathrm{d}^{-1}$ and $+0.186\,\mathrm{d}^{-1}$, respectively. This confidence interval is delineated by the dotted lines in Figs 1 and 2.

For illustrative purposes, we also plot the two gravity-mode pulsators having an identified dominant mode from their 5-months-long light curve assembled by the CoRoT space telescope. Even if their frequency precision is lower than the one deduced from 4-year duration *Kepler* light curves, they still occur in the vicinity of the *Kepler* pulsators with $(k, m) \neq (0, 1)$ modes. None of these stars (with open symbols) were used in the construction of the regression formula in Eq. (4).

2.4. The scaled buoyancy radius

For the observed dominant prograde dipole modes in the *Kepler* sample, we can use Eq. (1) to derive $\Pi_0\left(n + \alpha_g\right)$, where we use the mode frequencies and the determined rotation frequencies f_{rot} as input. The results of this analysis are shown in Fig. 3. Here, the derived 1-σ confidence intervals were propagated from the confidence intervals of f_{rot}, derived using stratified residual bootstrapping (Davison & Hinkley 1997). The relative scatter of the $\Pi_0\left(n + \alpha_g\right)$ values is larger than of the f_{rot} values, as reflected by a lower Pearson correlation coefficient of 0.542.

While most *Kepler* sample stars are in agreement with the confidence regions, a few outliers with measured mode frequencies between 1 and $1.2\,\mathrm{d}^{-1}$ occur. These stars from Li et al. (2020) are SPB stars based on their T_{eff} and our definition. They have anomalously high Π_0 values, which may result from an overestimated f_{rot} value propagating into the derived high $\Pi_0\left(n + \alpha_g\right)$ values above 4.5 d.

3. Application to a *Gaia* sample

Hey & Aerts (2024, their Fig. 6) found a distinct ridge in the stacked amplitude periodograms of the gravity-mode pulsators, characteristic for prograde dipole modes as also found for the *Kepler* γ Dor pulsators by Li et al. (2020). Among the 15,692 *Gaia* DR3 gravity-mode pulsators modelled by Mombarg et al. (2024b), we now define a sub-sample with the aim to select a maximum number of stars with a high probability of having a dominant prograde dipole mode in the TESS FFI light curve.

We require that *(i)* the amplitudes and frequencies of the dominant pulsations in the *Gaia* DR3 light curves are ≥ 4 mmag and $\leq 3.2\,\mathrm{d}^{-1}$, respectively (Aerts et al. 2023), *(ii)* they were classified by Hey & Aerts (2024) as γ Dor or SPB star or else as hybrid gravity/pressure mode pulsator, in all of these three cases with a probability above 50 %, *(iii)* the dominant frequencies measured from the *Gaia* and TESS data differ less than $0.1\,\mathrm{d}^{-1}$ (Hey & Aerts 2024), *(iv)* $\log(L/L_\odot) \geq 0$, and *(v)* $G_{Gaia} \leq 13$ mag. These stringent constraints deliver a sub-sample of 2,497 pulsators among those with parameters from evolutionary modelling by Mombarg et al. (2024b), notably their mass $M_\star$, convective core mass m_{cc}, radius $R_\star$, and evolutionary stage defined as the ratio of the hydrogen mass fraction remaining in the convective core compared to the initial value at birth, X_c/X_{ini}.

Following Hey & Aerts (2024), Fig. 4 shows the stacked periodograms of these 2,497 gravity-mode pulsators based on their TESS FFI light curves. A prominent ridge occurs, very similar to the one found for stars with dominant identified $(k, m) = (0, 1)$ modes from *Kepler* light curves by Li et al. (2020). This lends support to our assumption that these *Gaia* gravity-mode pulsators have a dominant prograde dipole gravito-inertial mode. In the remainder of this work we reasonably assume that all the 2,497 stars in our current sub-sample with periodogram shown in Fig. 4 fulfil the mode identification $(k, m) = (0, 1)$.

We now rely on the relations derived from the *Kepler* gravity-mode pulsators deduced in the previous Section to infer the near-core rotation rates f_{rot} and scaled buoyancy radius $\Pi_0\left(n + \alpha_g\right)$ for the 2,497 stars in the *Gaia* DR3 sub-sample. Uncertainties for these two inferred quantities are estimated using the confidence intervals defined in Sect. 2.3 and taking the frequency differences $|f_{\mathrm{dom},Gaia} - f_{\mathrm{dom,TESS}}|$ as an additional systematic observational error for f_{dom}, which we then propagate forward using the chain rule.

A first result, represented by the histograms in Fig. 5, is that the distributions of the dominant mode frequencies and of f_{rot} values are similar to those of the much smaller *Kepler* sample of γ Dor stars in Li et al. (2020) when we limit it to stars with dominant mode of amplitude above 4 mmag. Li et al. (2020) derived the near-core rotation from the slope of a period spacing pattern consisting of a series of prograde dipole gravito-inertial modes of consecutive radial order, following the method designed by Van Reeth et al. (2016). Here, we do not have such period spacing patterns and we only make use of the dominant mode in the blue ridge in Fig. 4 and the recipe in Eq. (4). As can be seen in Fig. 5, the distribution of f_{rot} achieved in this simplified way for our large *Gaia* sample of gravity-mode pulsators is fully in line with the one of the *Kepler* γ Dor pulsators.

Recall that we have purposefully excluded the low-frequency regime in the recipe, because the ultra-slow rotators among the gravity-mode pulsators do not comply with the linear relationship in Eq. (4). The dominant mode of all the 2,497 *Gaia* gravity-mode pulsators thus have a spin parameter placing them into the sub-inertial regime. The values shown in the bottom panel of Fig. 5 are in line with those of the 63 best characterised *Kepler* pulsators with spin parameters, Rossby numbers, and stiffness values in Aerts et al. (2021).

At the high frequency end, we excluded stars with f_{dom} above $3.2\,\mathrm{d}^{-1}$, reflected by the shorter tail in the distribution of the spin parameter in the bottom panel of Fig. 5. We thus find by construction that none of the isolated gravity-mode pulsators in our *Gaia* sample of field stars are expected to rotate close to their critical rate, justifying the use of the TAR for the recipe in Eq. (4). We quantify this qualitative statement in Sect. 4. Here, we just note that at least some of the γ Dor pulsators still embedded in their birth cluster are known to rotate faster, as was found for the ~ 100 Myr-old young open cluster NGC 2516. Li et al. (2024) identified 11 gravity-mode pulsators in this cluster and found most of them to have near-core rotation frequencies $f_{\mathrm{rot}} \simeq 3\,\mathrm{d}^{-1}$, which is faster than the rotation rates we find for the population of isolated galactic *Gaia* field pulsators.

In Fig. 6 we place the stars in the Hertzsprung-Russell (HR) diagram by colour-coding their markers according to their f_{rot} and $\Pi_0\left(n + \alpha_g\right)$ values. The pulsators cover a broad range in effective temperature and luminosity, reflecting a wide range in stellar masses, which we determine in Sect. 4. While the near-core rotation rates and scaled buoyancy radii of the stars hotter than 8500 K appear to be randomly distributed, those of the stars within the γ Dor instability region (shown in the inset) seem to correlate with $\log T_{\mathrm{eff}}$, in such a way that f_{rot} and $\Pi_0(n + \alpha_g)$ decrease and increase with $\log T_{\mathrm{eff}}$, respectively.

The 26 best modelled *Kepler* SPB stars did not reveal any correlation between $\log T_{\mathrm{eff}}$ and the dominant oscillation mode

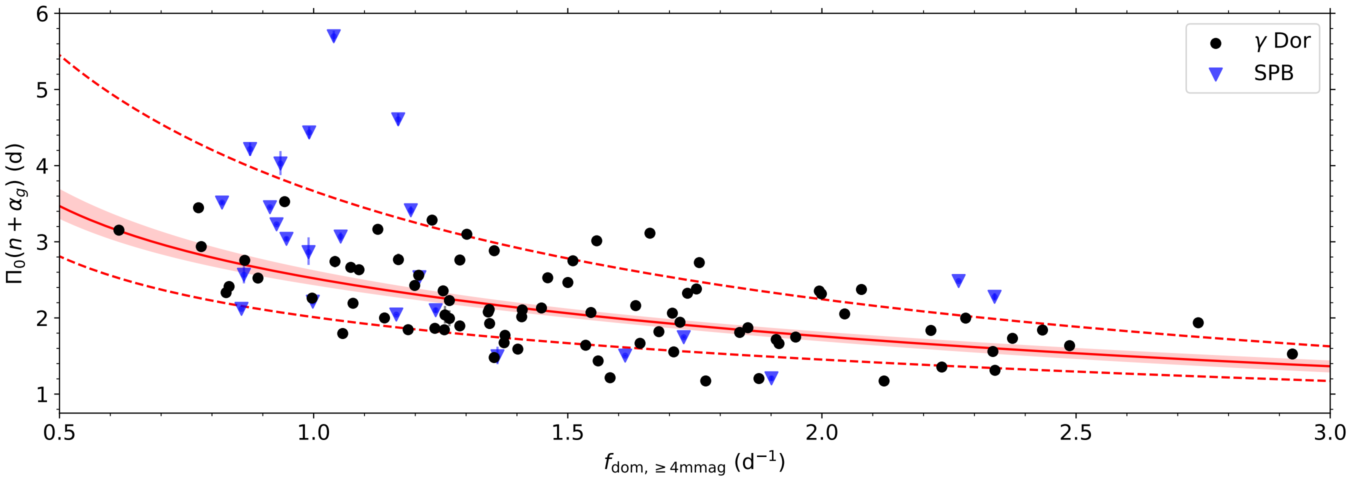

Fig. 3: The derived quantity $\Pi_0(n+\alpha_g)$ plotted as a function of the dominant prograde dipole gravity-mode frequency with amplitude above 4 mmag ($f_{\mathrm{dom},\,\geq 4\,\mathrm{mmag}}$) for 105 γ Dor and SPB stars from Li et al. (2020) and Pedersen et al. (2021). The symbols have the same meaning as in Fig. 1. The relation given by Eq. (3) is shown by the red line, while the shaded area shows the 1-σ uncertainty region. The dashed lines mark the 1-σ confidence region, propagated forward from the confidence regions of the f_{rot} values.

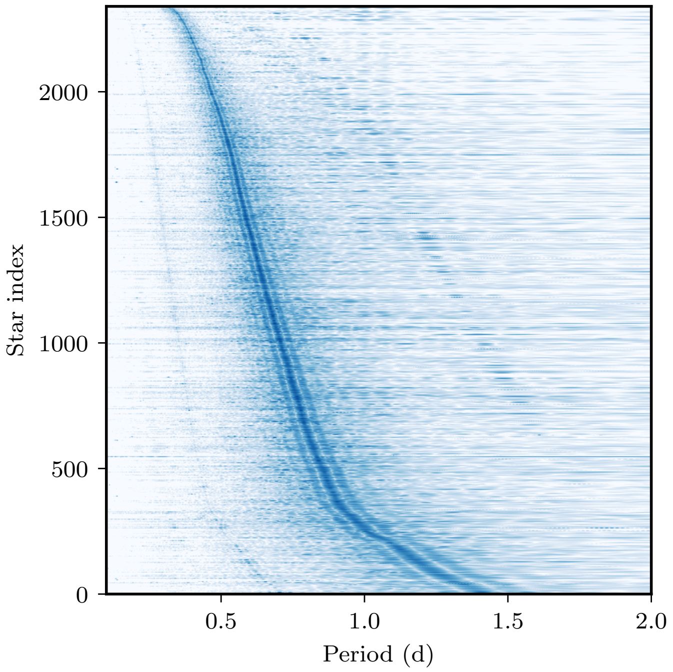

Fig. 4: Stacked periodogram of the 2,497 sample stars calculated for the TESS light curves from Hey & Aerts (2024). Each row corresponds to the amplitude spectrum of one star in the gravity-mode sub-sample treated here, sorted by the dominant mode period. For all these 2,497 pulsators, the dominant mode period occurs in the ridge of prograde dipole gravito-inertial $(k, m) = (0, 1)$ modes.

frequency, in line with earlier ground-based studies of 13 SPB pulsators (see Supplementary Material of Pedersen et al. 2021). We confirm this conclusion here for the much larger *Gaia* sample. This follows from simple linear regression analyses of the form $y = a \log T_{\mathrm{eff}} + b$, where y is taken to be f_{dom}, f_{rot}, and $\Pi_0\left(n+\alpha_g\right)$, respectively. We also repeat the regression for the inverse quantities and for the 10-base logarithm. We dedicate Appendix A to two illustrations on the (lack of) correlations between these three seismic quantities and the effective temperature for our *Gaia* sample. The linear regressions applied to the stars above the γ Dor instability strip lead to insignificant coefficients (a, b) for all of f_{dom}, f_{rot}, and $\Pi_0\left(n+\alpha_g\right)$, albeit they have low R^2 values as anticipated. The three relationships with $\log T_{\mathrm{eff}}$ are graphically depicted in the three scatter plots in Fig. A.1.

Table 1: Value of all coefficients differing significantly from zero (at p-value of 5%) for linear regressions between the listed dependent variables y and $\log T_{\mathrm{eff}}$, following the prescription $y = a \log T_{\mathrm{eff}} + b$.

y	a	b	r_{Pearson}	R^2
f_{dom}	$22.2^{+0.7}_{-0.7}$	$-83.9^{+2.6}_{-2.5}$	0.426	0.162
f^{-1}_{dom}	$-9.6^{+0.3}_{-0.3}$	$37.74^{+1.16}_{-1.11}$	−0.426	0.171
${}^{10}\log\left(f_{\mathrm{dom}}\right)$	$6.5^{+0.2}_{-0.2}$	$-24.7^{+0.7}_{-0.7}$	0.426	0.169
f_{rot}	$18.6^{+0.7}_{-0.7}$	$-70.5^{+2.7}_{-2.7}$	0.400	0.155
f^{-1}_{rot}	$-18.5^{+0.8}_{-0.8}$	$72.4^{+3.1}_{-2.9}$	-0.400	0.166
${}^{10}\log\left(f_{\mathrm{rot}}\right)$	$8.3^{+0.3}_{-0.3}$	$-32.1^{+1.2}_{-1.2}$	0.400	0.164
$\Pi_0\left(n+\alpha_g\right)$	$-16.3^{+1.5}_{-1.5}$	$64.9^{+6.0}_{-5.8}$	−0.250	0.187
$\left(\Pi_0\left(n+\alpha_g\right)\right)^{-1}$	$3.9^{+0.4}_{-0.4}$	$-14.5^{+1.4}_{-1.4}$	0.249	0.186
${}^{10}\log\left(\Pi_0\left(n+\alpha_g\right)\right)$	$-3.5^{+0.3}_{-0.3}$	$13.9^{+1.4}_{-1.2}$	−0.249	0.188

Li et al. (2020, their Fig. 15) did not find any correlation between the oscillation periods of the $(k, m) = (0, 1)$ modes and $\log T_{\mathrm{eff}}$ for their sample of *Kepler* γ Dor stars. No clear correpondence between Π_0 and $\log T_{\mathrm{eff}}$ was found either. We do find weak correlations from our much larger *Gaia* sample but the comparisons are not equivalent. Indeed, Li et al. (2020) were able to identify the radial orders of the modes from detected period spacing patterns for each of the pulsators. Here, we do not

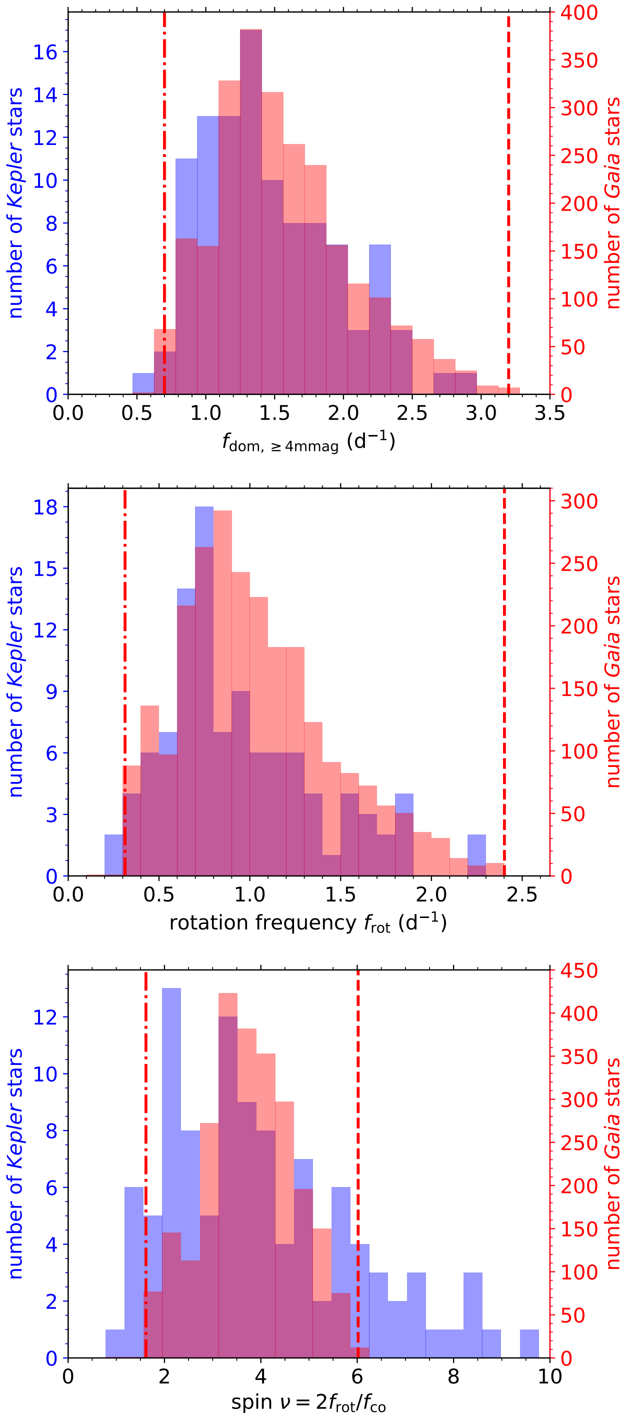

Fig. 5: Histograms of the dominant frequency of observed $(k, m) = (0, 1)$ modes revealing an amplitude above 4 mmag (top), of the near-core rotation frequency f_{rot} (middle), and of the spin parameter of the dominant mode (bottom) for the *Kepler* sample from Li et al. (2020, blue, left y-axis) and for our *Gaia* sample using Eq. (4) (red, right y-axis). The red dash-dotted and dashed lines mark the lower and upper boundaries for the *Gaia* sample, following from our selection criterion demanding that $f_{\mathrm{dom}} \in [0.7, 3.2]\,\mathrm{d}^{-1}$. Note the major increase in the number of pulsators thanks to *Gaia*, from comparison of the two y-axes ranges.

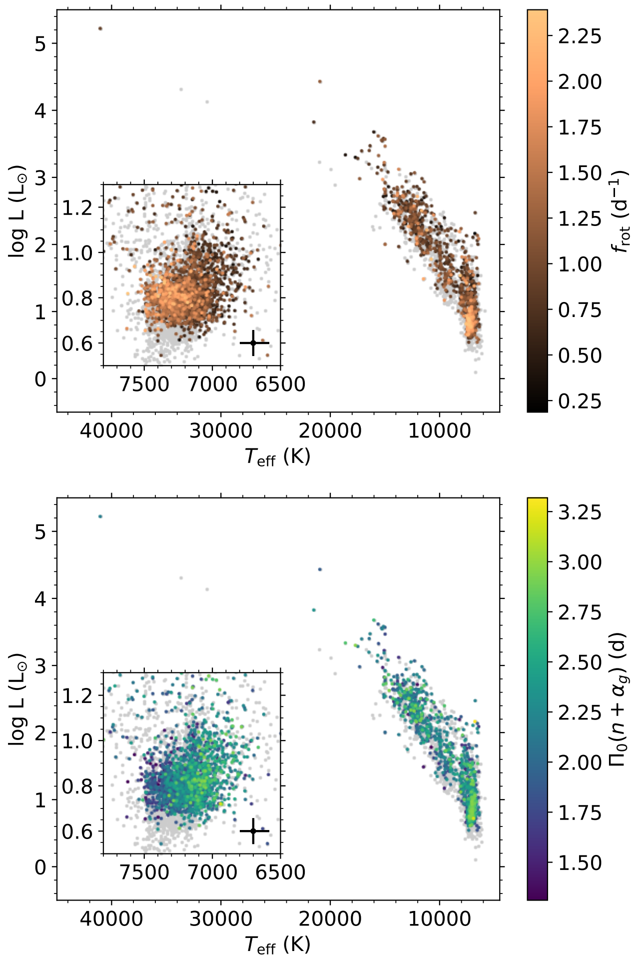

Fig. 6: The 2,497 selected *Gaia* DR3 gravity-mode pulsators in the HR diagram, with markers coloured according to their f_{rot} (top) and $\Pi_0(n + \alpha_g)$ values (bottom). The other stars of the entire sample consisting of 15,692 pulsators from Mombarg et al. (2024b) are shown by the grey markers. The inset axes show close-ups of the γ Dor instability region. Typical 3σ (average) error margins are shown by the black bars in the inset.

have any information on the radial order n of the dominant mode, so we cannot make use of the buoyancy radius Π_0 itself. Rather, we must use a scaled value including the unknown factor $(n+\alpha_g)$. Because we expect weak correlations between the three seismic quantities and log T_{eff} at best, we compute Pearson's correlation coefficients and conduct simple linear regressions. We do so with Monte Carlo sampling analyses for 10,000 iterations to assess the uncertainties. We select the stars with T_{eff} values between 6810 K and 7540 K following the local target density in the HR diagram in Fig. 6. In this way we ensure there to be at least 3 sample stars per 10 K within this T_{eff} range. In each iteration, we sample new values for log T_{eff}, f_{dom}, f_{rot}, and $\Pi_0(n + \alpha_g)$ for 85 % of the selected targets and fit linear, inverse, and logarithmic relations using Theil-Sen estimators (e.g., Theil 1950; Sen 1968). The results are summarised in Table 1. Although the R^2 values are low, as anticipated from the earlier *Kepler* results by Li et al. (2020), we find that f_{dom}, f_{rot}, and $\Pi_0(n+\alpha_g)$ all correlate modestly but significantly with log T_{eff}. The linear, inverse, and logarithmic regressions are illustrated in Fig. A.2. The positive a values in Table 1 point to a positive correlation between f_{dom}

and $\log T_{\rm eff}$, and by implication also between $f_{\rm rot}$ and $\log T_{\rm eff}$. These are well visible in Fig. A.2. On the other hand, the negative a value for $\Pi_0(n+\alpha_g)$ points to an anti-correlation with $\log T_{\rm eff}$ (see bottom panel of Fig. A.2). The weaker correlation occurs because of the wider asymmetrical confidence regions for this quantity as revealed in Fig. 3.

While the gravity-mode pulsators above the γ Dor instability region cover a wide range of stellar masses (Mombarg et al. 2024b, see also Sect. 4), those inside the narrow instability region have similar mass. This allows us to probe the evolution of these stars more easily (e.g., Mombarg et al. 2021; Fritzewski et al. 2024a) than the one of the less populated SPB sample. The modest yet significant linear decrease of $f_{\rm rot}$ as $\log T_{\rm eff}$ decreases for the γ Dor pulsators offers observational input to evaluate angular momentum transport theories and simulations as these stars evolve along the main sequence (e.g., Ouazzani et al. 2019; Aerts et al. 2019; Aerts 2021). Even if we could compute more complex statistical models than the simple linear ones used here, we refrain from doing so as long as we do not have the outcome of forward modelling based on fitting individual identified modes from grids of models with a variety of input physics as done for SPB stars by Pedersen et al. (2021). Indeed, Li et al. (2020, their Fig. 16) have illustrated that the connection between $f_{\rm rot}$, Π_0 and $T_{\rm eff}$ is complex and depends on the details of transport processes in the stellar interior as the stars evolve. We plan to achieve more advanced asteroseismic and statistical modelling in future work, by fully exploiting a considerable number of the identified modes from the TESS light curves of suitable γ Dor pulsators, rather than working with only the dominant mode as done here for the large *Gaia* sample. The results in Table 1 are promising to undertake such time-consuming modelling in the future.

Finally, even if the correlation is weak, we find that the scaled buoyancy radius $\Pi_0(n+\alpha_g)$ increases with decreasing $\log T_{\rm eff}$. This is contrary to Π_0 itself, which decreases as the star cools (e.g., Mombarg et al. 2019; Ouazzani et al. 2019). We thus find observational evidence of an increase in the radial order of the dominant excited mode as the γ Dor stars evolve.

4. Grid-based forward modelling

Mombarg et al. (2024a) and Fritzewski et al. (2024a) illustrated how measured values of the near-core rotation frequency and Π_0 provide useful extra constraints, in addition to the luminosity and effective temperature of a star, for stellar modelling based on evolutionary tracks. In these two studies, the modelling had the purpose of determining the stellar mass $M_\star$, the core overshooting leading to $m_{\rm cc}$, and age via its proxy $X_{\rm c}/X_{\rm ini}$. Such evolutionary modelling is a lot less cumbersome (but also less powerful) than detailed asteroseismic modelling of individual mode frequencies (e.g., Moravveji et al. 2015, 2016; Mombarg et al. 2020, 2021; Pedersen et al. 2021). This simplified evolutionary modelling by Mombarg et al. (2024a) and Fritzewski et al. (2024a) was done by relying on grids of stellar evolution models calibrated to γ Dor star asteroseismology computed by Mombarg (2023).

In recent applications of gravity-mode asteroseismic modelling, the near-core rotation frequency of the star was derived from 4-years long *Kepler* light curves. These typically lead to much better precision for $f_{\rm rot}$ compared to the precision of $\sim 20\%$ we achieve here from applying Eq. (4) to the measured $f_{\rm dom}$, after identification of the mode as $(k,m)=(0,1)$ in the sub-inertial regime. Here we investigate whether the addition of an estimated near-core rotation frequency from just the dominant pulsation frequency helps to constrain the fundamental stellar parameters $M_\star$, $m_{\rm cc}$, $R_\star$, and $X_{\rm c}/X_{\rm ini}$.

We apply the same methodology as presented in Mombarg et al. (2024b), where a conditional neural flow trained on a grid of rotating stellar evolution models computed with `MESA` (Paxton et al. 2011, 2013, 2015, 2018, 2019; Jermyn et al. 2023) is used as an interpolator. We refer to Mombarg et al. (2024b) for the details on how this methodology works. For the subsample of stars with a measured $f_{\rm rot}$ obtained in this work, we re-derive their $M_\star$, $m_{\rm cc}$, $R_\star$ and $X_{\rm c}/X_{\rm ini}$ by adding $f_{\rm rot}$ as a third observational constraint, in addition to the two observables $\log T_{\rm eff}$ and $\log(L/L_\odot)$ used for the modelling by Mombarg et al. (2024b). As in that paper, we rely on two extensive grids of stellar models, for values of the metallicity equal to $Z = 0.0045$ ([M/H] $= -0.5$) and $Z = 0.014$ ([M/H] $= 0.0$). These two metallicities were chosen because we do not have a homogeneously derived measurement of the metallicity for all the sample stars. The two grids encapsulate the measured range of Z for gravity-mode pulsators having a metallicity estimate from high-resolution ground-based spectroscopy (Gebruers et al. 2021) and from *Gaia* spectroscopy (de Laverny et al. 2024). In addition to these two grids from Mombarg et al. (2024b), we computed a third grid for $Z = 0.008$ ([M/H] $= -0.25$) and trained a conditional neural flow on this grid, following the same methodology as described in that paper. From the perspective of position in the HR diagram, 2375 pulsators fall into the lowest-metallicity grid, 2439 for the intermediate-metallicity grid and 2464 in the solar metallicity grid. We work with these stars from here onwards.

Figure 7 shows the difference in the derived fundamental stellar quantities depending on whether $f_{\rm rot}$ is included as an additional constraint or not, for the 2464 pulsators captured by the solar metallicity grid. As can be seen in the top-left panel, the derived stellar mass is consistent between the two cases. The largest scatter is observed in the evolutionary stage ($X_{\rm c}/X_{\rm ini}$, bottom-left panel), which is harder to constrain than the mass as it depends strongly on (unknown) element mixing in the models. In the context of ensemble modelling of gravity-mode pulsators, we find that $f_{\rm rot}$ derived from Eq. (4) applied to the *Gaia* light curves helps to refine the determination of the evolutionary stage of the star from rotating stellar models. Furthermore, with the inclusion of $f_{\rm rot}$, we achieve slightly more precise estimates of $X_{\rm c}/X_{\rm ini}$, going from average (absolute) uncertainties of 0.10-0.08 to 0.08-0.06. In case of the convective core mass (top-right panel) and radius (bottom-right panel), the majority of the stars with the largest difference still have measurements consistent within the 68% confidence interval. The average uncertainties $m_{\rm cc}/M_\star$ and $\log(R_\star/R_\odot)$ remain approximately the same when $f_{\rm rot}$ is included in the modelling or not. This re-affirms that estimation of $f_{\rm rot}$ can be decoupled from forward asteroseismic modelling as emphasized by Van Reeth et al. (2016), Ouazzani et al. (2017) and Aerts et al. (2018).

The comparative results for the 2375 pulsators covered by the lower-metallicity grids are similar, keeping in mind that the mass, luminosity, and metallicity are tightly connected for main-sequence stars (see their strong relationships deduced by Mombarg et al. 2024b). We omit them here for brevity, but they are shown visually in Figs B.1 and B.2 in Appendix A. Given that we do not have measurements of Z for the sample stars, we provide the stellar parameters for the three grids in electronic format at the CDS, following the format in Tables B.1, B.2, and B.3 (see also footnote to the title of the paper).

The differences in the stellar parameters deduced from the grid modelling for the stars treated by the three grids reflect the systematic uncertainties for the (core) masses, radii, and evolu-

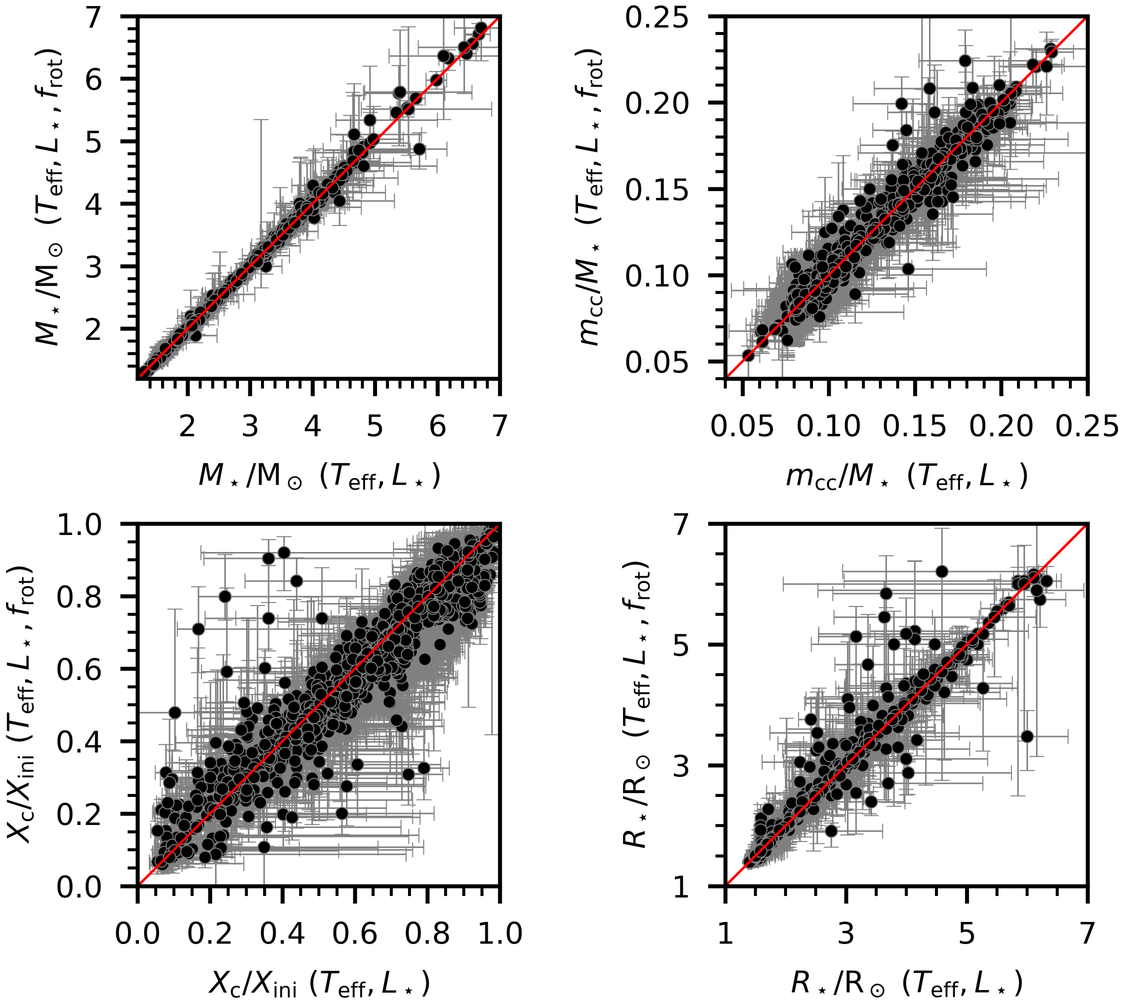

Fig. 7: Derived measurements for the stellar mass (top left), the fractional convective core mass (top right), the core hydrogen-mass fraction compared to the initial hydrogen-mass fraction (bottom left), and the stellar radius (bottom right) of the 2464 gravity-mode pulsators modelled via the grid with solar metallicity. The quantities on the abscissa are derived using the effective temperature and luminosity as input, while for the quantities on the ordinate, the near-core rotation frequency is added as an extra observable. The red lines indicate perfect correspondence.

tionary stages induced solely by the differences of 0.0060 and 0.0095 in Z (-0.25 and -0.50 in [M/H]). Again, these differences are systematic following the tight (core) mass – luminosity – radius – metallicity relationships. They range up to $0.55\,\mathrm{M}_\odot$ in mass, up to $0.28\,\mathrm{M}_\odot$ in convective core mass, and from about $-0.25\,\mathrm{R}_\odot$ to $+0.25\,\mathrm{R}_\odot$ in radius. By construction, the evolutionary stages differ from each other because the grid having $Z = 0.0045$ was built up by Mombarg et al. (2024b) to make sure all observed stars are above the ZAMS and to encapsulate the range in unknown metallicity reported in the literature for gravity-mode pulsators, affecting the evolution appreciably. For the grid with $Z = 0.008$ the differences in $X_\mathrm{c}/X_\mathrm{ini}$ remain more modest for most stars, reaching up to 0.3 compared to the solar metallicity case. A visual representation of the distributions of these systematic differences for all the stars with overlapping grid solutions is shown in Fig. B.3 in Appendix A.

Finally, we also study the effect of having the higher-precision input of f_rot from the slope of a period-spacing pattern of dipole prograde modes based on 4-year *Kepler* light curves instead of the value based on just f_dom from *Gaia* DR3 light curves. We consider the 105 *Kepler* pulsators from Li et al. (2020) and Pedersen et al. (2021) used to construct Eq. (4) and shown in Fig. 1. We compute their luminosity and effective temperature in the same way as we did it for the *Gaia* sample and find 96 of the γ Dor stars with dominant $(k, m) = (0, 1)$ mode to be covered by the model grid with solar metallicity, while 3 of the SPB stars. We compare the results of the grid modelling based on the less precise *Gaia* f_rot and the more precise *Kepler* f_rot estimates for these 99 *Kepler* pulsators in Fig. 8. The four estimated parameters have very consistent values for almost all 99 pulsators.

Having deduced the stellar parameters from grid modelling, we are now able to come back to one of the main assumptions in our procedure, namely that the pulsators may rotate fast, yet such that the centrifugal force can still be neglected. The centrifugal force affects both the equilibrium models and the pulsation computations. The former become oblate spheroids rather than spheres, while the modes will not only get affected by the Coriolis force but as well by the centrifugal force $\sim \Omega^2$. To eval-

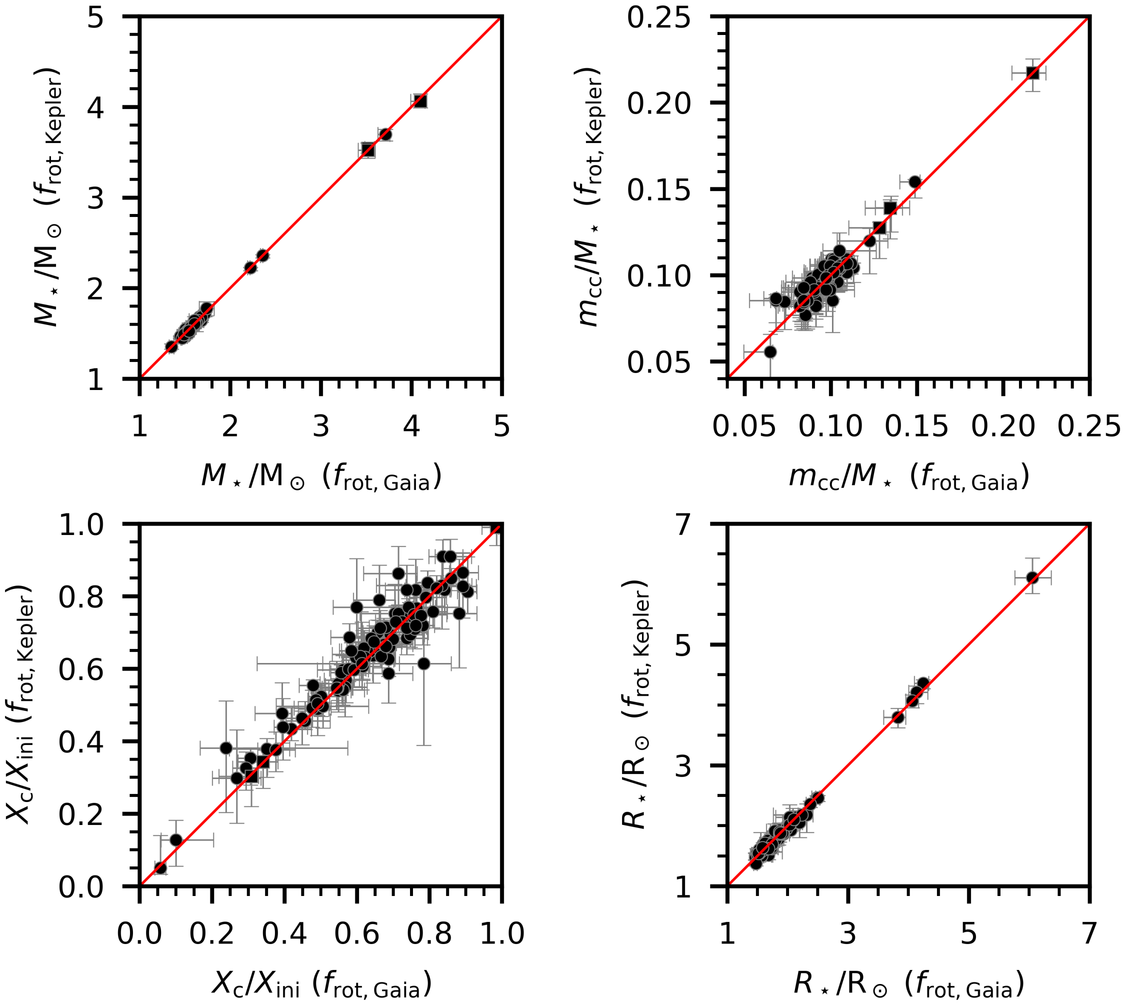

Fig. 8: Derived measurements for the stellar mass (top left), the fractional convective core mass (top right), the core hydrogen-mass fraction compared to the initial hydrogen-mass fraction (bottom left), and the stellar radius (bottom right) of 96 γ Dor stars (circles) and 3 SPB stars (squares) modelled via the grid with solar metallicity. The quantities are derived using the effective temperature, luminosity, and near-core rotation frequency from the dominant dipole prograde mode detected in the *Gaia* DR3 light curves (x-axis) versus the higher-precision value deduced from the slope of a period spacing pattern of dipole prograde modes of consecutive radial order following Li et al. (2020) and Pedersen et al. (2021) (y-axis).

uate the impact on the equilibrium models, we test at which fraction of the critical rotation rate the stars are rotating. We note that different definitions for the critical rotation rate are used in the literature, notably the Kepler and Roche critical rate. In practical applications, these differ by a factor up to 1.84 due to the use of the equatorial or polar radius of the star at the critical rate (see Rieutord et al. 2016; Aerts & Tkachenko 2024, for discussions). Here, we work with the cyclic Kepler critical rotation rate defined as $f_{\mathrm{crit}} \equiv \sqrt{GM_\star/(R_\star^{\mathrm{eq}})^3}$ and assume the derived radii of the stars to correspond with their equatorial value. This is an appropriate choice since we are dealing with stars having a dominant sectoral dipole mode in an observer's frame, which favours a more equator-on than pole-on view. We then use the mass result from the grid modelling to compute $f_{\mathrm{rot}}/f_{\mathrm{crit}}$ for all the pulsators in our *Gaia* sample. The values range from 0.7% to 25% and imply that the stars are not strongly deformed by the rotation according to the asteroseismic validity criteria for prograde modes adopted by Ballot et al. (2012) and Ouazzani et al. (2017). The latter authors, as well as Ballot et al. (2013) conclude that the centrifugal force can safely be ignored for the calculation of prograde dipole gravity modes when $f_{\mathrm{rot}}/f_{\mathrm{crit}} < 40\%$, which is fulfilled for all our sample stars. This justifies the use of the TAR also from the perspective of the stellar deformation due to the rotation.

Overall, our results reveal the great potential of using Eq. (4) to deduce f_{rot} and grid-based stellar parameter estimation based on just the value of the dominant mode frequency from *Gaia* light curves along with the effective temperature and luminosity. All these quantities are homogeneously computed and available from *Gaia* DR3 (and its future Data Releases DR4 and DR5). When coupled to an asteroseismically calibrated grid of stellar models as those in Mombarg et al. (2024b) and used here, these observables deliver stellar parameters calibrated by the star's internal properties via the observed dominant mode frequency. The only requirement for the procedure to work is the ability to identify pulsators with a dominant dipole prograde mode having its frequency in the frame co-rotating with the star, $f_{\rm co}$, in the sub-inertial regime of the frequency spectrum (spin parameter $\nu = 2 \cdot f_{\rm rot}/f_{\rm co} > 1$), while ensuring a modest rotational deformation of $f_{\rm rot}/f_{\rm crit} < 40\%$.

5. Near-core to surface rotation estimates

5.1. Evolution of the near-core rotation

Combining the results of the previous two sections, we can now study the near-core rotation frequency as a function of evolutionary stage. Asteroseismology has demonstrated that angular momentum transport from the deep interior to the envelope of stars happens more efficiently than anticipated from theories of transport processes adopted prior to the era of space asteroseismology (Ouazzani et al. 2019). It was also found that gravity-mode pulsators have low levels of near-core to surface rotation (Aerts et al. 2019; Li et al. 2020; Aerts 2021; Aerts & Tkachenko 2024, for observational summaries). Moreover, stars born with a radiative envelope lose angular momentum rapidly beyond the TAMS (at $X_c/X_{\rm ini} = 0$)), while their near-core rotation drops appreciably (Aerts 2021, Fig. 6).

In Fig. 9, we show the model-independent near-core rotation frequency, $f_{\rm rot}$, as a function of the model-dependent evolutionary stage for our sample of gravity-mode pulsators, for both grids. Thanks to the four times larger size of our *Gaia* population of pulsators with a measurement of $f_{\rm rot}$ compared to the Li et al. (2020) *Kepler* sample, and to our estimate of the evolutionary stage, we see a clear decline of the average near-core rotation frequency of the population as the stars evolve.

We fit uni-variate splines through bin-averaged $f_{\rm rot}$ values, where we select the optimal bin size in $X_{\rm c}' = X_{\rm c}/X_{\rm ini}$ according to Scott's rule (Scott 1979). This rule states that a histogram with bin size proportional to $3.49 \cdot \sigma/(N_{\rm points}^{1/3})$, where $N_{\rm points}$ is the number of points in the bins and σ the standard deviation assuming a normal distribution, is very efficient in approaching the true distribution. The smoothing factor for the splines is chosen such that higher values do no longer change the resulting derivative $\mathrm{d}f_{\rm rot}/\mathrm{d}X_{\rm c}'$. The derivatives of the fitted splines are shown in the bottom panel of Fig. 9. When assuming $Z = 0.014$, we find purely decreasing $f_{\rm rot}$ values during the main sequence. Despite the large range of near-core rotation frequencies per evolutionary stage – reflecting the variety of initial conditions at birth for this population of field stars – the average near-core rotation per bin in $X_c/X_{\rm ini}$ shows a gradual decline from the zero-age to the terminal-age main sequence, with roughly a factor of two.

Assuming $Z = 0.0045$, the results are less clear. We find that stars on average have an increasing $f_{\rm rot}$ (negative derivative) during the first part of the main sequence, followed by a decrease in $f_{\rm rot}$. Yet, we note that the part where $\mathrm{d}f_{\rm rot}/\mathrm{d}X_{\rm c}' < 0$ for $Z = 0.0045$ is severely undersampled and so we cannot rely on these results. However, the same decline of $f_{\rm rot}$ with a factor two as for the solar metallicity grid is obtained for the regime $X_{\rm c}/X_{\rm ini} < 0.5$ when the stars are modelled with the metal-poor grid. When assuming $Z = 0.008$, a similar trend in $\mathrm{d}f_{\rm rot}/\mathrm{d}X_{\rm c}'$ is observed.

Finally, we checked that the trends found become less clear but do not change globally when we split up the observed sample in stars with an initially growing convective core and stars whose convective core shrinks as of the ZAMS. The distinction between these two cases happens for masses between about $1.6\,{\rm M}_\odot$ and $1.8\,{\rm M}_\odot$, depending on the metallicity. We therefore conclude to have found observational evidence that the near-core rotation frequency of isolated gravity-mode field pulsators in the Milky Way decreases with a factor of about two by the time they

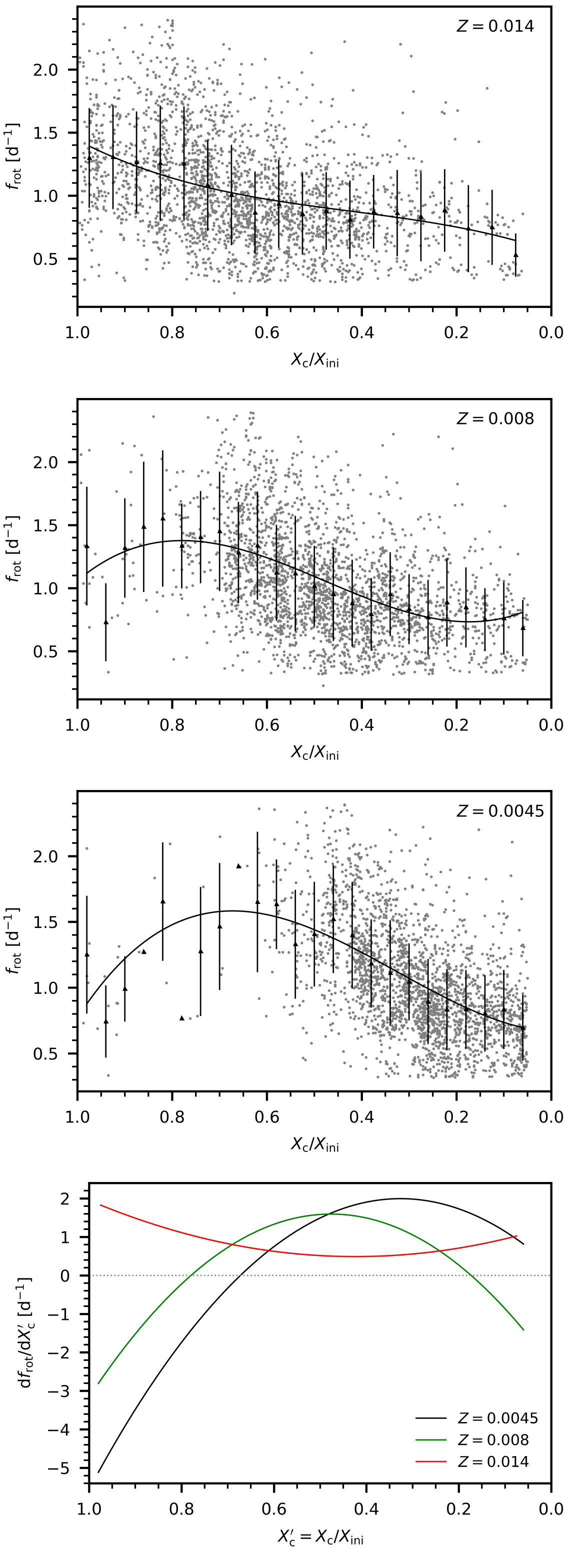

Fig. 9: Inferred near-core rotation frequencies of the *Gaia* gravity-mode pulsators plotted as a function of evolutionary stage (grey dots), assuming solar metallicity (2464 stars, top panel), [M/H] = −0.25 (2439 stars, 2nd panel), and [M/H] = −0.5 (2375 stars, 3rd panel). Solid lines indicate spline fits through binned averages (see text). The bottom panel shows the derivatives of the splines from the three upper panels, indicating the change in the near-core rotation frequency with respect to the fraction of hydrogen in the core. The dotted grey line separates positive and negative values.

will reach the TAMS if we consider all the well covered bins in Fig. 9, irrespective of the initial metallicity.

5.2. Limits on the surface rotation

Only 58 of the *Kepler* γ Dor stars also have a value for the surface rotation, measured from rotational modulation (Van Reeth et al. 2018; Li et al. 2020) and only 22 have a measurement of their averaged envelope rotation, $f_{\rm env}$, determined from identified rotational splitting (Kurtz et al. 2014; Saio et al. 2015; Keen et al. 2015; Li et al. 2019). For the SPB stars, information is even more restricted, with only one star having clear rotational splitting (Pápics et al. 2014) and a rotational profile throughout the star from frequency inversions (the 3.3 $\mathrm{M}_\odot$ SPB KIC 10526294, Triana et al. 2015). These limited observational constraints on differential near-core to surface rotation in main-sequence stars of intermediate and high mass (as summarised by Aerts 2021, Fig. 6) restrict our ability to improve angular momentum transport theories, as these rely on the gradient of the rotation profile throughout the star (Ouazzani et al. 2019; Aerts et al. 2019).

We are unable to assess the envelope or surface rotation from the *Gaia* light curves. However, we can give a lower limit for the cyclic surface rotation frequency, $f_{\rm surf}$, from the radius estimates shown in Fig. 7 for those stars with a measurement of the spectral line broadening offered by the *Gaia* spectroscopy (Frémat et al. 2023). Aerts et al. (2023) showed the *Gaia* `vbroad` parameter to capture the joint effect of time-independent rotational line broadening and time-dependent tangential pulsational broadening due to gravity modes. Moreover, pulsational line broadening of gravity-mode pulsators is typically only a small fracion of the rotational broadening for moderate to fast rotators (De Cat & Aerts 2002; Aerts et al. 2004; De Cat et al. 2006). Hence *Gaia*'s `vbroad` measurement is a meaningful approximation of $2\pi R_\star \cdot f_{\rm surf} \cdot \sin i$ for such stars, where i is the (unknown) inclination angle of the rotation axis of the star in the line-of-sight.

A total of 307 of our sample stars have a significant `vbroad` measurement, by which we mean it is above zero at 1-σ level, and a radius estimate from the solar metallicity grid. For the lower-metallicity grids it concerns 305 stars for $Z = 0.008$ and 292 stars for $Z = 0.0045$. Using the radius estimates from the grid modelling, we compute $f_{\rm surf} \cdot \sin i$ from `vbroad`. As this is a lower limit for the true surface rotation frequency $f_{\rm surf}$, we obtain an upper limit for the near-core to surface differential rotation from calculating $f_{\rm rot}/(f_{\rm surf} \cdot \sin i)$. The results are illustrated in Fig. B.4 and reveal values up to 5.4, irrespective of the assumption about the metallicity.

So far, asteroseismology of single γ Dor stars covering the mass range $[1.3, 1.9]\,\mathrm{M}_\odot$ has shown them all to have quasi-rigid rotation at the level of $f_{\rm rot}/f_{\rm surf} \in [0.9, 1.1]$ if such a measurement is available (Li et al. 2020; Aerts 2021, for a summary). Our work increases the mass range of stars with an estimate of differential rotation, even if we can provide only an upper limit. Indeed, of the 307 gravity-mode pulsators presented in Fig. B.4, 29 have a mass between 2.0 $\mathrm{M}_\odot$ and 4.4 $\mathrm{M}_\odot$ when adopting solar metallicity. However, the unknown factor $\sin i$ and the large uncertainty of `vbroad` do not allow us to deduce stricter constraints than just a rough upper limit for $f_{\rm rot}/f_{\rm surf}$. Measurements of the actual ratio $f_{\rm rot}/f_{\rm env}$ can be investigated from detailed analyses of the TESS light curves for the hybrid low-order pressure and high-order gravity mode pulsators in our sample. This will be taken up in future work.

6. Conclusions and outlook

In this work, we derive the internal rotation frequency of 2,497 gravity-mode pulsators discovered recently from *Gaia* DR3 light curves. These field stars cover the mass range from 1.3 $\mathrm{M}_\odot$ to about 7 $\mathrm{M}_\odot$ and the entire main sequence. We provide an easy-to-apply procedure to deduce their near-core rotation frequency. Our linear regression recipe is based on the dominant prograde dipole oscillation mode found in the *Gaia* DR3 light curves. The 2,497 *Gaia* pulsators have near-core rotation rates ranging from 0.3 d^{-1} ($\simeq 3.5\,\mu$Hz) to 2.4 d^{-1} ($\simeq 27.8\,\mu$Hz), with a distribution in line with those of *Kepler* gravity-mode pulsators. All these *Gaia* pulsators have an identified dominant dipole prograde mode in the sub-inertial frequency regime with spin parameters ranging from about 2 to 6. They cover a ratio of the near-core rotation rate to the Keplerian critical rate from 0.7% to 25%. Their stellar parameters were deduced from asteroseismically calibrated grids of rotating stellar models. With our work, we quadruple the sample size of intermediate-mass dwarfs with a measurement of the near-core rotation frequency in the transition layer between the convective core and the radiative envelope.

The weakest point of the grid modelling performed for the *Gaia* sample is the quite large uncertainty for the evolutionary stage of the stars, quantified as the central hydrogen mass fraction over the initial value, $X_c/X_{\rm ini}$. The reason is that we do not have a good estimate of the initial metallicity of the pulsators, preventing us to assign an age to the stars based on their $X_c/X_{\rm ini}$ value. This can perhaps be overcome from future detailed asteroseismic modelling based on a measurement of abundances from high-resolution spectroscopy coupled to the fitting of numerous identified oscillation mode frequencies from grids of stellar models built with a variety of choices for the input physics. The study by Pedersen et al. (2021) is so far the only one that achieved such an asteroseismic age calibration for gravity-mode pulsators on the main sequence. The authors considered eight grids of models with different input physics for the transport processes, but their study only covered 26 modelled SPB stars. Future similar work for a large sample with the most promising among our *Gaia* pulsators from their complete list of significant TESS oscillation frequencies is on the horizon.

For 307 pulsators in the sample, we derive an upper limit of the radial differential rotation between the boundary of the convective core and the surface, by relying on the *Gaia* DR3 `vbroad` observable combined with the radius estimate from the grid modelling. We find values up to 5.4. These results cover the mass range of $[1.3, 4.4]\,\mathrm{M}_\odot$ and constitute an interesting subsample to calibrate stellar evolution theory and angular momentum transport theories for rotating main-sequence stars with a convective core and a radiative envelope. This is of particular interest during the initial $\sim$ 20% of the main sequence. In order to understand such early phases of stellar evolution, it is needed to deduce high-precision values for $X_c/X_{\rm ini}$. An excellent way to achieve this, as well as calibrate age-dating from $X_c/X_{\rm ini}$, is to perform asteroseismic modelling of gravity-mode pulsators in detached binaries and/or open clusters. Such modelling work was done for a few binaries (Schmid & Aerts 2016; Sekaran et al. 2021; Kemp et al. 2024) and also for the open cluster UBC 1 (Fritzewski et al. 2024b). It is currently ongoing for the very young ($\simeq$ 100 Myr) open cluster NGC 2516, in which Li et al. (2024) discovered 9 γ Dor and 2 SPB pulsators rotating at half their critical Keplerian rotation rate. This is a higher internal rotation regime than the one covered by our sample of *Gaia* field pulsators.

Finally, we point to the large potential of future *Gaia* Data Releases. Combining these data with high-cadence high-precision space photometry from the ongoing TESS and future PLATO (Rauer et al. 2024) missions will allow us to scale up the work presented here to millions of pulsators, instead of thousands. Our recipe in Eq. (4) to deduce the near-core rotation of pulsators with a dominant prograde dipole gravito-inertial mode having a mass above 1.3 $M_\odot$ is suitable to facilitate fast asteroseismic grid modelling. At the same time, it is also a particularly handy and relevant tool for exoplanet host studies in terms of the angular momentum properties of the hottest among the main-sequence star-planet systems.

Acknowledgements. We thank the referee for the useful detailed suggestions, which helped us to improve the presentation of our work. CA is grateful to Maarten Dirickx, Toon De Prins and Thomas Ceulemans for helping her with compiler issues. The research leading to these results has received funding from the KU Leuven Research Council (grant C16/18/005: PARADISE) and from the European Research Council (ERC) under the Horizon Europe programme (Synergy Grant agreement N°101071505: 4D-STAR). While partially funded by the European Union, views and opinions expressed are however those of the authors only and do not necessarily reflect those of the European Union or the European Research Council. Neither the European Union nor the granting authority can be held responsible for them. CA also acknowledges the Belgian Federal Science Policy Office (BELSPO) for their financial support in the framework of the PRODEX Programme of the European Space Agency (ESA), facilitating the exploitation of the *Gaia* data. JSGM acknowledges funding fron the French Agence Nationale de la Recherche (ANR), under grant MASSIF (ANR-21-CE31-0018-02). The authors appreciated valuable comments from Dominic Bowman, Dario Fritzewski, and Mathijs Vanrespaille on an early version of the manuscript.

References

Aerts, C. 2021, Reviews of Modern Physics, 93, 015001
Aerts, C., Augustson, K., Mathis, S., et al. 2021, A&A, 656, A121
Aerts, C., Christensen-Dalsgaard, J., & Kurtz, D. W. 2010, Asteroseismology, Springer-Verlag Heidelberg
Aerts, C., Cuypers, J., De Cat, P., et al. 2004, A&A, 415, 1079
Aerts, C., Mathis, S., & Rogers, T. M. 2019, ARA&A, 57, 35
Aerts, C., Molenberghs, G., & De Ridder, J. 2023, A&A, 672, A183
Aerts, C., Molenberghs, G., Michielsen, M., et al. 2018, ApJS, 237, 15
Aerts, C. & Tkachenko, A. 2024, A&A, 692, R1
Aerts, C., Van Reeth, T., & Tkachenko, A. 2017, ApJ, 847, L7
Audenaert, J. & Tkachenko, A. 2022, A&A, 666, A76
Ballot, J., Lignières, F., Prat, V., Reese, D. R., & Rieutord, M. 2012, in Astronomical Society of the Pacific Conference Series, Vol. 462, Progress in Solar/Stellar Physics with Helio- and Asteroseismology, ed. H. Shibahashi, M. Takata, & A. E. Lynas-Gray, 389
Ballot, J., Lignières, F., & Reese, D. R. 2013, in Lecture Notes in Physics, Berlin Springer Verlag, ed. M. Goupil, K. Belkacem, C. Neiner, F. Lignières, & J. J. Green, Vol. 865, 91
Beck, P. G., Bedding, T. R., Mosser, B., et al. 2011, Science, 332, 205
Beck, P. G., Montalban, J., Kallinger, T., et al. 2012, Nature, 481, 55
Bedding, T. R., Mosser, B., Huber, D., et al. 2011, Nature, 471, 608
Bétrisey, J., Eggenberger, P., Buldgen, G., Benomar, O., & Bazot, M. 2023, A&A, 673, L11
Bouabid, M. P., Dupret, M. A., Salmon, S., et al. 2013, MNRAS, 429, 2500
Chaboyer, B. & Zahn, J. P. 1992, A&A, 253, 173
Córsico, A. H., Althaus, L. G., Miller Bertolami, M. M., & Kepler, S. O. 2019, A&A Rev., 27, 7
Davison, A. C. & Hinkley, D. V. 1997, Bootstrap Methods and their Application, Cambridge Series in Statistical and Probabilistic Mathematics (Cambridge University Press)
De Cat, P. & Aerts, C. 2002, A&A, 393, 965
De Cat, P., Eyer, L., Cuypers, J., et al. 2006, A&A, 449, 281
de Laverny, P., Recio-Blanco, A., Aerts, C., & Palicio, P. A. 2024, A&A, 691, A182
Degroote, P., Aerts, C., Baglin, A., et al. 2010, Nature, 464, 259
Deheuvels, S., Ballot, J., Beck, P. G., et al. 2015, A&A, 580, A96
Deheuvels, S., Ballot, J., Eggenberger, P., et al. 2020, A&A, 641, A117
Deheuvels, S., Doğan, G., Goupil, M. J., et al. 2014, A&A, 564, A27
Deheuvels, S., García, R. A., Chaplin, W. J., et al. 2012, A&A, 756, 19
Dhouib, H., Prat, V., Van Reeth, T., & Mathis, S. 2021a, A&A, 652, A154
Dhouib, H., Prat, V., Van Reeth, T., & Mathis, S. 2021b, A&A, 656, A122
Di Mauro, M. P., Ventura, R., Cardini, D., et al. 2016, ApJ, 817, 65
Dupret, M.-A., Belkacem, K., Samadi, R., et al. 2009, A&A, 506, 57
Eggenberger, P., Deheuvels, S., Miglio, A., et al. 2019a, A&A, 621, A66
Eggenberger, P., den Hartogh, J. W., Buldgen, G., et al. 2019b, A&A, 631, L6
Eggenberger, P., Moyano, F. D., & den Hartogh, J. W. 2022, A&A, 664, L16
Frémat, Y., Royer, F., Marchal, O., et al. 2023, A&A, 674, A8
Fritzewski, D. J., Aerts, C., Mombarg, J. S. G., Gossage, S., & Van Reeth, T. 2024a, A&A, 684, A112
Fritzewski, D. J., Van Reeth, T., Aerts, C., et al. 2024b, A&A, 681, A13
Fuller, J., Piro, A. L., & Jermyn, A. S. 2019, MNRAS, 485, 3661
Gaia Collaboration, De Ridder, J., Ripepi, V., et al. 2023, A&A, 674, A36
García, R. A. & Ballot, J. 2019, Living Reviews in Solar Physics, 16, 4
Garcia, S., Van Reeth, T., De Ridder, J., et al. 2022, A&A, 662, A82
Gebruers, S., Straumit, I., Tkachenko, A., et al. 2021, A&A, 650, A151
Gehan, C., Mosser, B., Michel, E., Samadi, R., & Kallinger, T. 2018, A&A, 616, A24
Guzik, J. A., Kaye, A. B., Bradley, P. A., Cox, A. N., & Neuforge, C. 2000, ApJ, 542, L57
Heger, A., Langer, N., & Woosley, S. E. 2000, ApJ, 528, 368
Hekker, S. & Christensen-Dalsgaard, J. 2017, A&A Rev., 25, 1
Henneco, J., Van Reeth, T., Prat, V., et al. 2021, A&A, 648, A97
Hermes, J. J., Gänsicke, B. T., Kawaler, S. D., et al. 2017, ApJS, 232, 23
Hey, D. & Aerts, C. 2024, A&A, 688, A93
Jermyn, A. S., Bauer, E. B., Schwab, J., et al. 2023, ApJS, 265, 15
Keen, M. A., Bedding, T. R., Murphy, S. J., et al. 2015, MNRAS, 454, 1792
Kemp, A., Tkachenko, A., Torres, G., et al. 2024, A&A, 689, A164
Kurtz, D. W. 2022, ARA&A, 60, 31
Kurtz, D. W., Saio, H., Takata, M., et al. 2014, MNRAS, 444, 102
Lee, U. & Saio, H. 1987, MNRAS, 224, 513
Lee, U. & Saio, H. 1997, ApJ, 491, 839
Li, G., Aerts, C., Bedding, T. R., et al. 2024, A&A, 686, A142
Li, G., Bedding, T. R., Murphy, S. J., et al. 2019, MNRAS, 482, 1757
Li, G., Van Reeth, T., Bedding, T. R., et al. 2020, MNRAS, 491, 3586
Maeder, A. 2009, Physics, Formation and Evolution of Rotating Stars, Springer Verlag, Heidelberg
Maeder, A. & Meynet, G. 2000, ARA&A, 38, 143
Mathis, S. 2013, Transport Processes in Stellar Interiors, ed. M. Goupil, K. Belkacem, C. Neiner, F. Lignières, & J. J. Green, Vol. 865, 23
Mathis, S. & Prat, V. 2019, A&A, 631, A26
Miglio, A., Montalbán, J., Noels, A., & Eggenberger, P. 2008, MNRAS, 386, 1487
Mombarg, J. S. G. 2023, A&A, 677, A63
Mombarg, J. S. G., Aerts, C., & Molenberghs, G. 2024a, A&A, 685, A21
Mombarg, J. S. G., Aerts, C., Van Reeth, T., & Hey, D. 2024b, A&A, 691, A131
Mombarg, J. S. G., Dotter, A., Van Reeth, T., et al. 2020, ApJ, 895, 51
Mombarg, J. S. G., Van Reeth, T., & Aerts, C. 2021, A&A, 650, A58
Mombarg, J. S. G., Van Reeth, T., Pedersen, M. G., et al. 2019, MNRAS, 485, 3248
Moravveji, E., Aerts, C., Pápics, P. I., Triana, S. A., & Vandoren, B. 2015, A&A, 580, A27
Moravveji, E., Townsend, R. H. D., Aerts, C., & Mathis, S. 2016, ApJ, 823, 130
Mosser, B., Benomar, O., Belkacem, K., et al. 2014, A&A, 572, L5
Mosser, B., Goupil, M. J., Belkacem, K., et al. 2012, A&A, 548, A10
Mosser, B., Vrard, M., Belkacem, K., Deheuvels, S., & Goupil, M. J. 2015, A&A, 584, A50
Moyano, F. D., Eggenberger, P., Mosser, B., & Spada, F. 2023a, A&A, 673, A110
Moyano, F. D., Eggenberger, P., & Salmon, S. J. A. J. 2024, A&A, 681, L16
Moyano, F. D., Eggenberger, P., Salmon, S. J. A. J., Mombarg, J. S. G., & Ekström, S. 2023b, A&A, 677, A6
Ouazzani, R. M., Lignières, F., Dupret, M. A., et al. 2020, A&A, 640, A49
Ouazzani, R. M., Marques, J. P., Goupil, M. J., et al. 2019, A&A, 626, A121
Ouazzani, R.-M., Salmon, S. J. A. J., Antoci, V., et al. 2017, MNRAS, 465, 2294
Pamyatnykh, A. A. 1999, Acta Astron., 49, 119
Pápics, P. I., Briquet, M., Baglin, A., et al. 2012, A&A, 542, A55
Pápics, P. I., Moravveji, E., Aerts, C., et al. 2014, A&A, 570, A8
Pápics, P. I., Tkachenko, A., Van Reeth, T., et al. 2017, A&A, 598, A74
Paxton, B., Bildsten, L., Dotter, A., et al. 2011, ApJS, 192, 3
Paxton, B., Cantiello, M., Arras, P., et al. 2013, ApJS, 208, 4
Paxton, B., Marchant, P., Schwab, J., et al. 2015, ApJS, 220, 15
Paxton, B., Schwab, J., Bauer, E. B., et al. 2018, ApJS, 234, 34
Paxton, B., Smolec, R., Schwab, J., et al. 2019, ApJS, 243, 10
Pedersen, M. G. 2022a, ApJ, 940, 49
Pedersen, M. G. 2022b, ApJ, 930, 94
Pedersen, M. G., Aerts, C., Pápics, P. I., et al. 2021, Nature Astronomy, 5, 715
Rauer, H., Aerts, C., Cabrera, J., et al. 2024, Experimental Astronomy, under review, arXiv:2406.05447
Rieutord, M., Espinosa Lara, F., & Putigny, B. 2016, Journal of Computational Physics, 318, 277
Saio, H., Kurtz, D. W., Murphy, S. J., Antoci, V. L., & Lee, U. 2018, MNRAS, 474, 2774
Saio, H., Kurtz, D. W., Takata, M., et al. 2015, MNRAS, 447, 3264

Saio, H., Takata, M., Lee, U., Li, G., & Van Reeth, T. 2021, MNRAS, 502, 5856
Schmid, V. S. & Aerts, C. 2016, A&A, 592, A116
Scott, D. W. 1979, Biometrika, 66, 605
Sekaran, S., Tkachenko, A., Abdul-Masih, M., et al. 2020, A&A, 643, A162
Sekaran, S., Tkachenko, A., Johnston, C., & Aerts, C. 2021, A&A, 648, A91
Sen, P. K. 1968, Journal of the American Statistical Association, 63, 1379
Sepulveda, A. G., Huber, D., Li, G., et al. 2023, Research Notes of the American Astronomical Society, 7, 2
Sepulveda, A. G., Huber, D., Zhang, Z., et al. 2022, ApJ, 938, 49
Szewczuk, W. & Daszyńska-Daszkiewicz, J. 2017, MNRAS, 469, 13
Szewczuk, W. & Daszyńska-Daszkiewicz, J. 2018, MNRAS, 478, 2243
Szewczuk, W., Walczak, P., & Daszyńska-Daszkiewicz, J. 2021, MNRAS, 503, 5894
Theil, H. 1950, A rank-invariant method of linear and polynomial regression analysis, I, II, III, Nederl. Akad. Wetensch., Proc., 53, 386–392, 521–525, 1397–1412
Townsend, R. H. D. 2003, MNRAS, 340, 1020
Triana, S. A., Corsaro, E., De Ridder, J., et al. 2017, A&A, 602, A62
Triana, S. A., Moravveji, E., Pápics, P. I., et al. 2015, ApJ, 810, 16
Van Reeth, T., Mombarg, J. S. G., Mathis, S., et al. 2018, A&A, 618, A24
Van Reeth, T., Tkachenko, A., & Aerts, C. 2016, A&A, 593, A120
Van Reeth, T., Tkachenko, A., Aerts, C., et al. 2015a, A&A, 574, A17
Van Reeth, T., Tkachenko, A., Aerts, C., et al. 2015b, ApJS, 218, 27
Wu, T., Li, Y., Deng, Z.-m., et al. 2020, ApJ, 899, 38
Xiong, D. R., Deng, L., Zhang, C., & Wang, K. 2016, MNRAS, 457, 3163
Zahn, J. P. 1992, A&A, 265, 115

Appendix A: Correlations between seismic quantities and the effective temperature

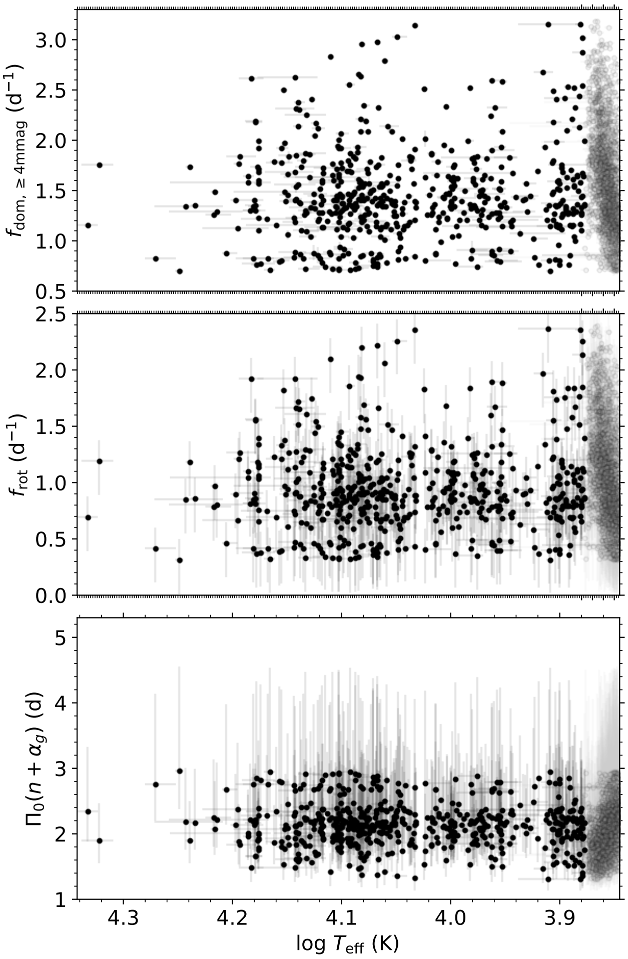

Fig. A.1: The dominant mode frequency (top) and inferred near-core rotation frequency $f_{\rm rot}$ (middle) and $\Pi_0\left(n+\alpha_g\right)$ (bottom) plotted as a function of log $T_{\rm eff}$ for pulsators above (black) and within (grey) the γ Dor instability region. The hot targets in black cover a wide mass range and do not show any significant correlation with log $T_{\rm eff}$.

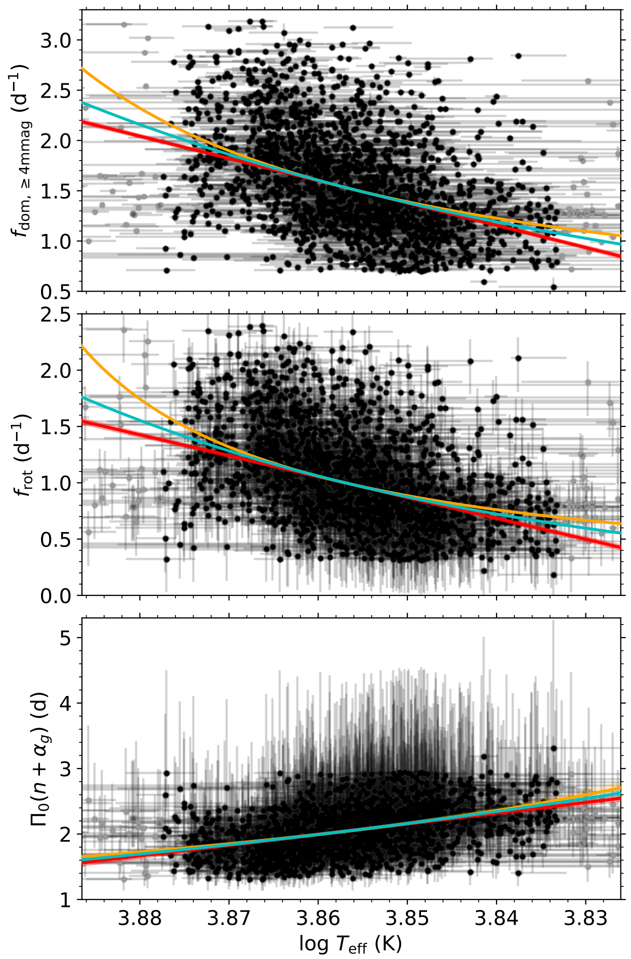

Fig. A.2: The dominant mode frequency (top) and inferred near-core rotation frequency $f_{\rm rot}$ (middle) and $\Pi_0\left(n+\alpha_g\right)$ (bottom) plotted as a function of log $T_{\rm eff}$ for pulsators within (black) and outside (grey) the γ Dor instability region. The orange, cyan, and red lines show the results of inverse, logarithmic, and linear regression analyses for the black dots with coefficients listed in Table 1, respectively. The dearth of stars in the upper panel at $f_{\rm dom,\,\geq 4\,mmag} \simeq 1\,{\rm d}^{-1}$ is due to the spectral window of the TESS data as illustrated by Hey & Aerts (2024).

Appendix B: Extra figures and tables connected with Sect. 4

In this Appendix, we show some extra figures discussed in the main text, as well as the format of two data tables, which are only available electronically via the CDS.

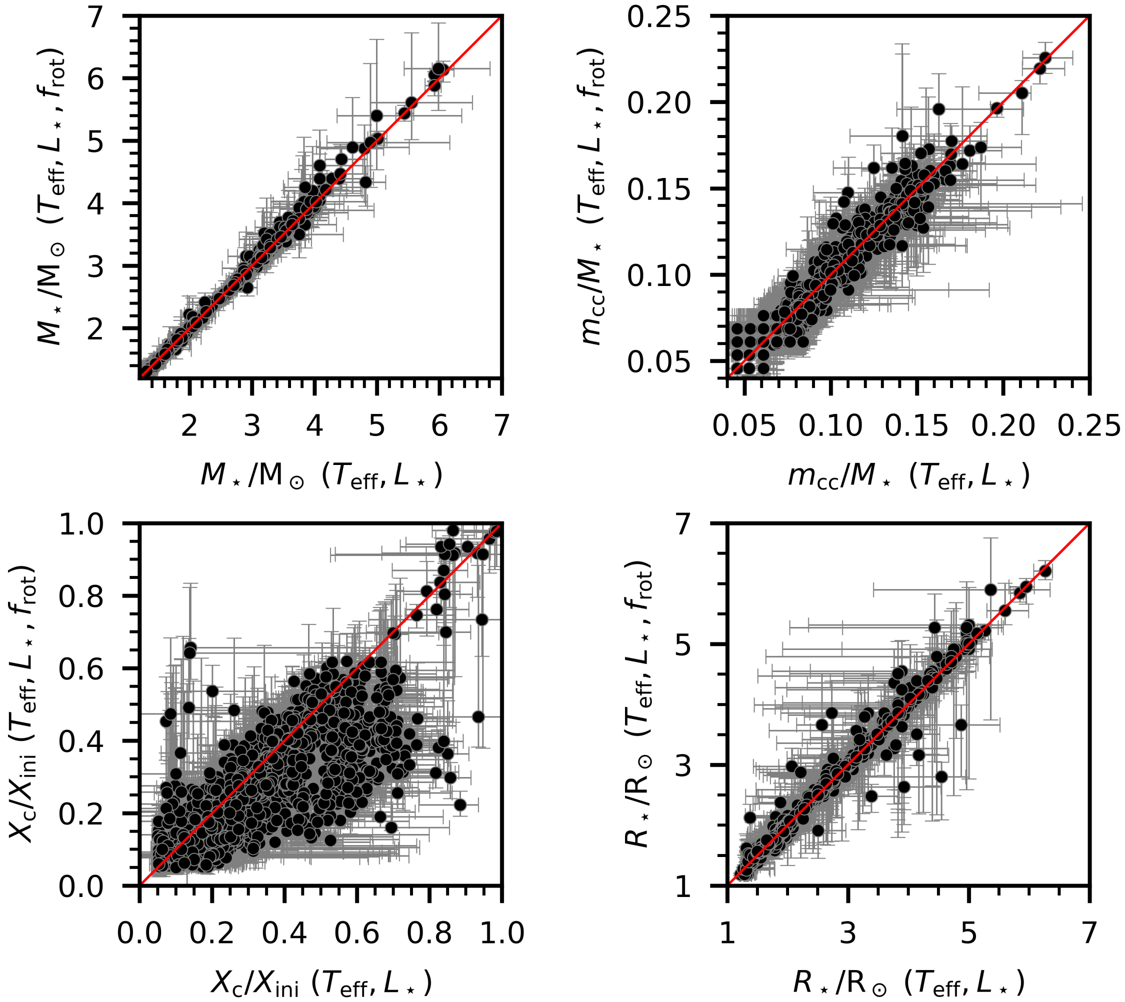

Fig. B.1: Similar to Fig. 7, but for the 2375 gravity-mode pulsators modelled via the [M/H] = −0.5 grid.

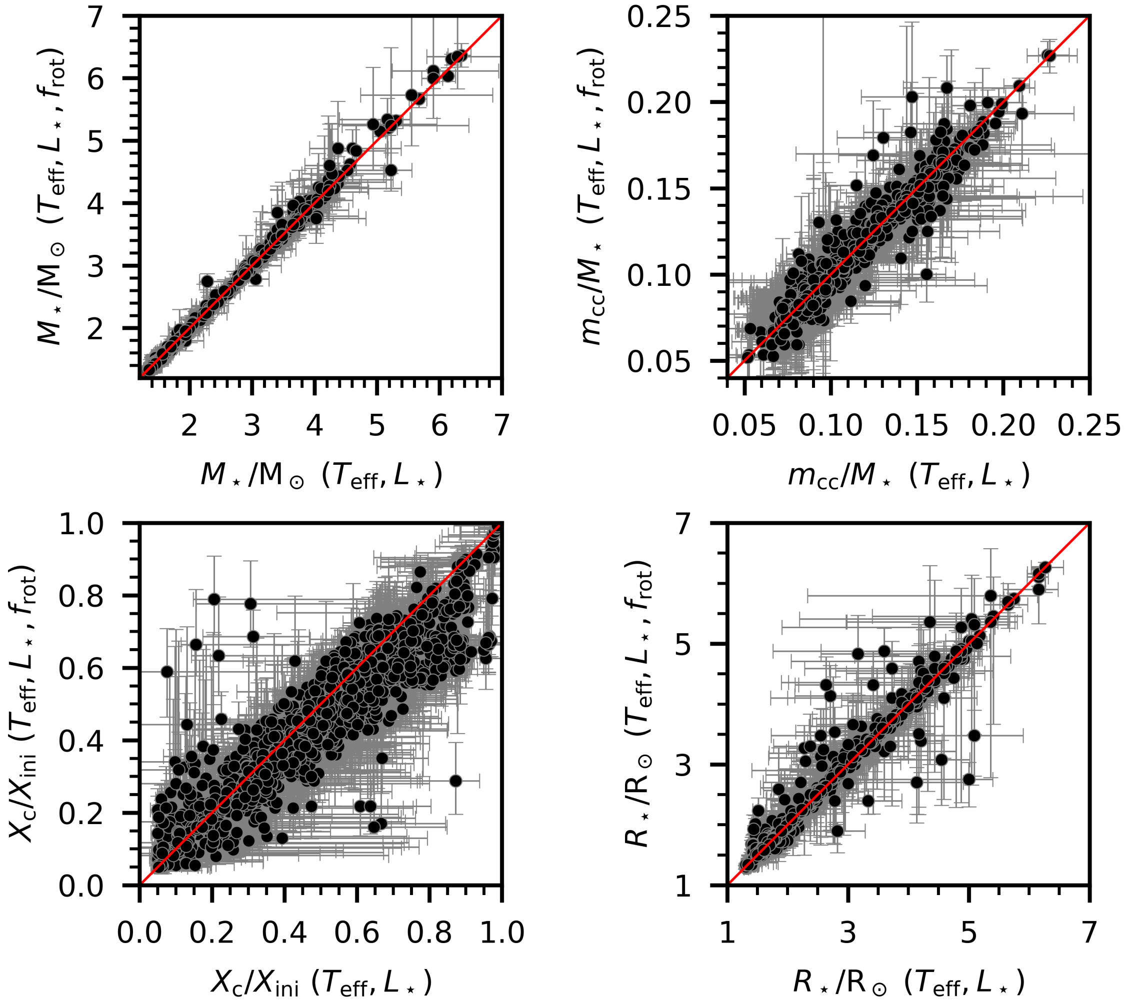

Fig. B.2: Similar to Fig. 7, but for the 2439 gravity-mode pulsators modelled via the [M/H] = −0.25 grid.

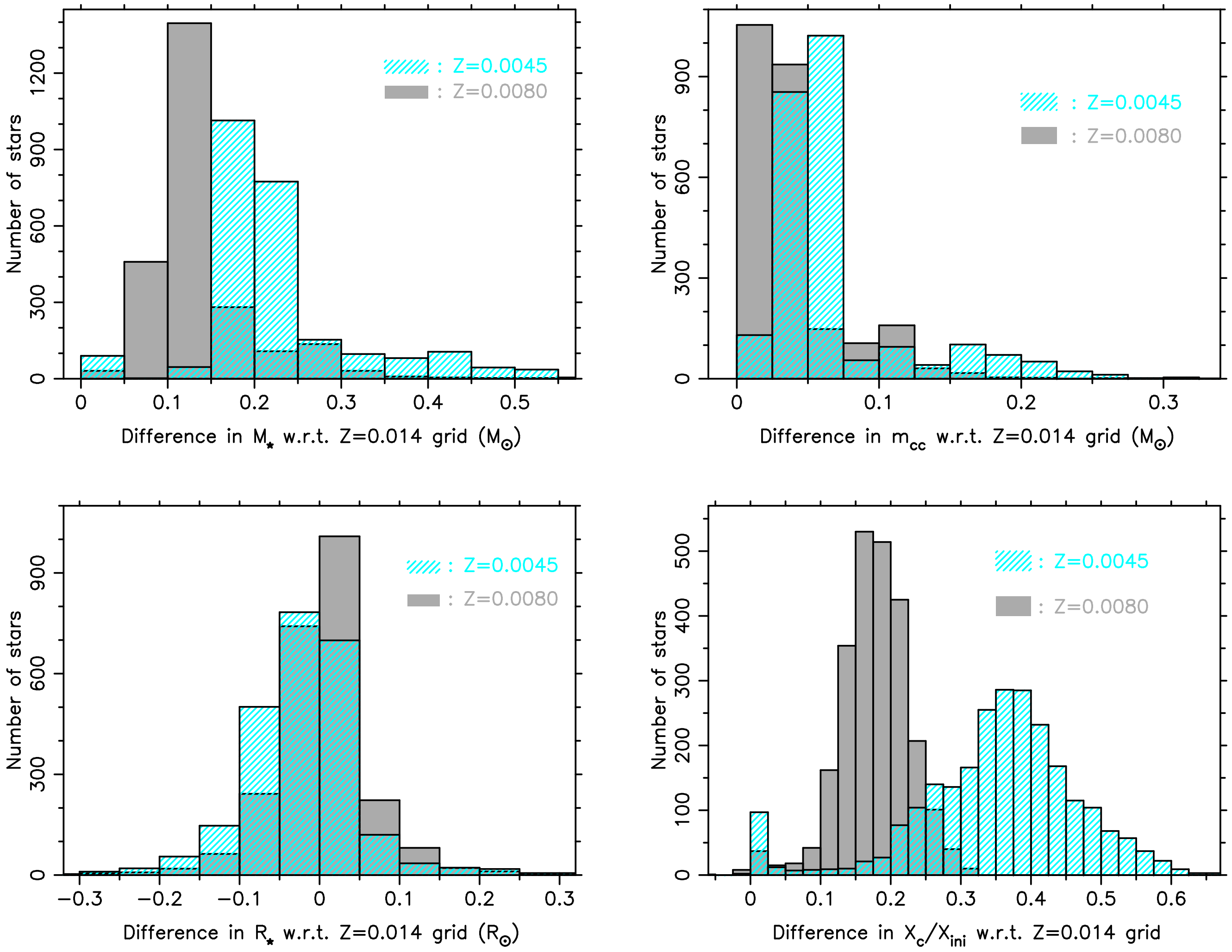

Fig. B.3: Differences in estimates from the grid modelling for the mass (upper left), convective core mass (upper right), radius (lower left), and evolutionary stage (lower right) due to the change in metallicity. The differences arise from the values for $Z = 0.014$ minus those for $Z = 0.008$ (grey) and $Z = 0.0045$ (cyan), respectively. These systematic shifts reflect the well-known luminosity–mass-radius–metallicity relationships for main-sequence stars (cf. Mombarg et al. 2024b).

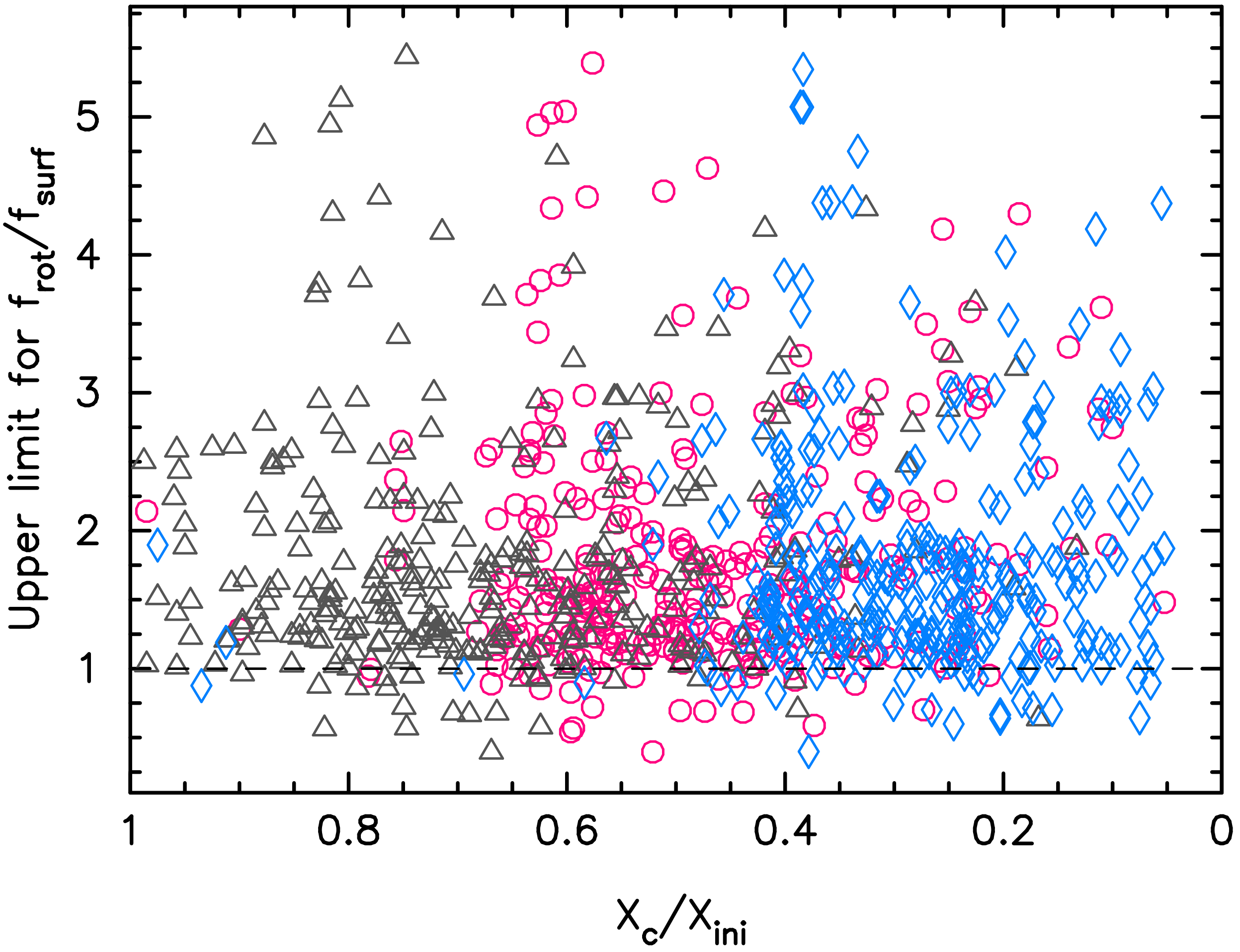

Fig. B.4: Upper limits for the near-core to envelope rotation rate deduced from *Gaia* DR3 measurements of `vbroad` available for 307 gravity-mode pulsators in the sample of pulsators, all of which have a radius estimate from the solar-metallicity grid (grey triangles). The $Z = 0.008$ and $Z = 0.0045$ grids deliver this upper limit for 305 (pink circles) and 292 (blue diamonds) of the stars. All these upper limits are significant at 1-σ level but have large uncertainty (up to 100%) for many of the stars due to the large errors of `vbroad` (not shown for visibility reasons). In particular we note that the errors are such that the stars with value below the dashed line all have an uncertainty region including values above 1.0.

Table B.1: Parameters of the gravity-mode pulsators covered by the solar metallicity grid. When available, the error estimates of a quantity X are given as a_X and b_X in the notation $X^{+b_X}_{-a_X}$. Frequencies are given in the unit d^{-1} while the stellar (core) mass and radius are given in solar units. The quantity $f_{\rm co-rot}$ is the frequency of the dominant gravito-inertial mode in a frame of reference co-rotating with $f_{\rm rot}$, while 'spin' stands for the spin parameter of the dominant mode in the region just outside the convective core. The full table is available online via the CDS.

Gaia DR3 ID	$f_{\rm rot}$	$a_{f_{\rm rot}}$	$b_{f_{\rm rot}}$	$\mathrm{M}_\star$	$a_{\mathrm{M}_\star}$	$b_{\mathrm{M}_\star}$	$X_{\rm c}/X_{\rm ini}$	$a_{X_{\rm c}/X_{\rm ini}}$	$b_{X_{\rm c}/X_{\rm ini}}$	$m_{\rm cc}$	$a_{m_{\rm cc}}$	$b_{m_{\rm cc}}$	$\log(R_\star/R_\odot)$	$a_{\log(R_\star/R_\odot)}$	$b_{\log(R_\star/R_\odot)}$	$f_{\rm co-rot}$	spin	$f_{\rm surf}\cdot\sin i$	$f_{\rm rot}/(f_{\rm surf}\cdot\sin i)$
164941072177351424	0.93767	0.16430	0.12293	3.77256	0.07590	0.04231	0.51880	0.06017	0.03535	0.60150	0.04841	0.02017	0.53383	0.01765	0.01497	0.51010	3.67642	—	—
185403705126528256	1.16134	0.16431	0.12293	1.50733	0.01523	0.01123	0.80702	0.04583	0.03352	0.13033	0.01222	0.00585	0.18797	0.01018	0.00689	0.55408	4.19196	—	—
⋮	⋮	⋮	⋮	⋮	⋮	⋮	⋮	⋮	⋮	⋮	⋮	⋮	⋮	⋮	⋮	⋮	⋮	⋮	⋮
200619262425969024	1.64651	0.16497	0.12382	1.48797	0.03052	0.01000	0.89223	0.07543	0.04644	0.12030	0.02328	0.00319	0.17293	0.01266	0.01166	0.64949	5.07016	1.42700	1.15383
⋮	⋮	⋮	⋮	⋮	⋮	⋮	⋮	⋮	⋮	⋮	⋮	⋮	⋮	⋮	⋮	⋮	⋮	⋮	⋮

Table B.2: Same as Table B.1 but for the grid having Z = 0.0080. The full table is available online via the CDS.

Gaia DR3 ID	$f_{\rm rot}$	$a_{f_{\rm rot}}$	$b_{f_{\rm rot}}$	$\mathrm{M}_\star$	$a_{\mathrm{M}_\star}$	$b_{\mathrm{M}_\star}$	$X_{\rm c}/X_{\rm ini}$	$a_{X_{\rm c}/X_{\rm ini}}$	$b_{X_{\rm c}/X_{\rm ini}}$	$m_{\rm cc}$	$a_{m_{\rm cc}}$	$b_{m_{\rm cc}}$	$\log(R_\star/R_\odot)$	$a_{\log(R_\star/R_\odot)}$	$b_{\log(R_\star/R_\odot)}$	$f_{\rm co-rot}$	spin	$f_{\rm surf}\cdot\sin i$	$f_{\rm rot}/(f_{\rm surf}\cdot\sin i)$
164941072177351424	0.93767	0.16430	0.12293	3.52086	0.07890	0.05629	0.37845	0.05959	0.04983	0.48120	0.04536	0.03724	0.53008	0.01471	0.01843	0.51010	3.67642	—	—
185403705126528256	1.16134	0.16431	0.12293	1.37180	0.01456	0.02682	0.60652	0.05884	0.02316	0.12030	0.01738	0.00291	0.18797	0.00813	0.01017	0.55408	4.19196	—	—
⋮	⋮	⋮	⋮	⋮	⋮	⋮	⋮	⋮	⋮	⋮	⋮	⋮	⋮	⋮	⋮	⋮	⋮	⋮	⋮
200619262425969024	1.64651	0.16497	0.12382	1.35244	0.01544	0.01203	0.62155	0.04435	0.06126	0.10025	0.01923	0.00611	0.17669	0.01827	0.01008	0.64949	5.07016	1.41470	1.16386
⋮	⋮	⋮	⋮	⋮	⋮	⋮	⋮	⋮	⋮	⋮	⋮	⋮	⋮	⋮	⋮	⋮	⋮	⋮	⋮

Table B.3: Same as Table B.1 but for the grid having Z = 0.0045. The full table is available online via the CDS.

Gaia DR3 ID	$f_{\rm rot}$	$a_{f_{\rm rot}}$	$b_{f_{\rm rot}}$	$\mathrm{M}_\star$	$a_{\mathrm{M}_\star}$	$b_{\mathrm{M}_\star}$	$X_{\rm c}/X_{\rm ini}$	$a_{X_{\rm c}/X_{\rm ini}}$	$b_{X_{\rm c}/X_{\rm ini}}$	$m_{\rm cc}$	$a_{m_{\rm cc}}$	$b_{m_{\rm cc}}$	$\log(R_\star/R_\odot)$	$a_{\log(R_\star/R_\odot)}$	$b_{\log(R_\star/R_\odot)}$	$f_{\rm co-rot}$	spin	$f_{\rm surf}\cdot\sin i$	$f_{\rm rot}/(f_{\rm surf}\cdot\sin i)$
164941072177351424	0.93767	0.16430	0.12293	3.34662	0.07221	0.05528	0.28070	0.09347	0.03254	0.42105	0.06547	0.01727	0.54135	0.01826	0.01336	0.51010	3.67642	—	—
185403705126528256	1.16134	0.16431	0.12293	1.31372	0.01894	0.00624	0.37343	0.06841	0.03501	0.09023	0.00987	0.00860	0.19549	0.01133	0.00620	0.55408	4.19196	—	—
⋮	⋮	⋮	⋮	⋮	⋮	⋮	⋮	⋮	⋮	⋮	⋮	⋮	⋮	⋮	⋮	⋮	⋮	⋮	⋮
200619262425969024	1.64651	0.16497	0.12382	1.31372	0.01858	0.01000	0.34837	0.04428	0.06441	0.09023	0.01349	0.00586	0.19925	0.00852	0.01219	0.64949	5.07016	1.34308	1.22592
⋮	⋮	⋮	⋮	⋮	⋮	⋮	⋮	⋮	⋮	⋮	⋮	⋮	⋮	⋮	⋮	⋮	⋮	⋮	⋮